NUMERICAL INVESTIGATION OF STABILITY CHARACTERISTICS OF A JET IN COUNTERFLOW

by

SIDDARTH CHINTAMANI

Presented to the Faculty of the Graduate School of
The University of Texas at Arlington in Partial Fulfillment
of the Requirements
for the Degree of

DOCTOR OF PHILOSOPHY

THE UNIVERSITY OF TEXAS AT ARLINGTON

August 2017

To my parents, Usha and Ganesh, for without them I'm nothing.

To my loving brother, Bharath, for his support.

To my grand parents for being my first teachers.

To my uncle, Suresh Ketha, who inspires me to achieve big things in life.

ACKNOWLEDGEMENTS

I would like to express my sincere gratitude to my advisor, Dr. Brian Dennis for his academic advise, constant support and encouragement. I would like to thank Professors Kamesh Subbarao, Bo Wang, Zhen Han and Guojun Liao for serving on my committee. I am grateful to Dr. Subbarao for providing me valuable insights into this research work. I am also grateful to Dr. Luca Massa for providing me with research assistantship during the initial semesters of my PhD and showing me that academic research is fun and exciting.

I would like to acknowledge my friends from CFD lab, specifically Sandeep, James, Alok, Aditya, Ashkan, Manoj and Anirudh for all the inspiration and support. Special thanks to Sandeep for the early morning discussions and motivating me when I needed it the most. My thanks also go out to Nanda, Bryce, Pavan, Jason, Ghas, Rahul and Pallav for making this path to the degree fun and interesting.

Furthermore, I would like to acknowledge the financial support provided by the MAE Department through various fellowships and the computational resources provided by the Texas Advance Computing Center (TACC).

I am extremely grateful to my parents and grand parents for their constant love, encouragement and support. I would like to thank my brother for always being there for me as a friend. I would also like to thank my uncle, Suresh, my aunt, Sumana, and my cousins, Siri and Sam for their support. I also acknowledge the inspiration and help I recieved from my friends back in India, specifically Manohar.

August 9, 2017

ABSTRACT

NUMERICAL INVESTIGATION OF STABILITY CHARACTERISTICS OF A JET IN COUNTERFLOW

SIDDARTH CHINTAMANI, Ph.D.

The University of Texas at Arlington, 2017

Supervising Professor: Brian H Dennis

A jet in counterflow is a configuration in which a jet is issued into an opposing external stream of fluid. Some of the possible applications of this configuration include study of pollutant discharge into body of water, aerodynamic flame holder in after burner, reduction of drag and cooling of bluff body by ejecting a jet of coolant gas into counterflowing stream, thrust vectoring of supersonic jets, sonic boom mitigation. The instability associated with flow reversal which is observed in this configuration of the jet leads to enhanced mixing. However, a detailed understanding of the dynamics and control is needed to make these applications practical.

The goal of this thesis is to perform global stability analysis of a jet in counterflow and understand the characteristics of its stability. Above the critical values of jet Reynolds number and the jet to counterflow velocity ratio, the flowfield becomes unstable and the jet tip oscillates at a low frequency. One of the objectives of this thesis is to find these critical values.

Hydrodynamic stability analysis involves the determination of eigenvalues of the perturbation equations, linearized about steady base flow and the corresponding

adjoint perturbation equations. When the flow is globally unstable, it is impossible to time-march to steady state. In this research, a feedback control technique known as selective frequency damping (SFD) is implemented. The parameters involved in the SFD method are adapted based on the solution to an optimization problem. However, the SFD method is not suitable for obtaining the base flows in the presence of unstable low frequency and stationary modes. In such a case, base flow solution is obtained using Newtons method.

The search for global modes is carried out using the block Krylov-Schur method. The Navier-Stokes equations, the linearized perturbation equations and the adjoint equations are numerically solved using the embedded boundary adaptive refinement strategy.

The effect of non-normality of the Navier-Stokes operator on the trasnient energy amplification of perturbations is evaluated. The structural sensitivity of the jet is obtained by computing the adjoint eigenmodes and the regions in the flowfield where the growth rate and frequency of leading eigenmode are most sensitive to forcing are identified.

TABLE OF CONTENTS

LIST OF FIGURES

LIST OF TABLES

CHAPTER 1

INTRODUCTION

1.1 Jet in counterflow

A jet in counterflow is a configuration in which a jet interacts with an opposing external stream of fluid. Figure (1.1) shows schematic of the time-averaged flowfield associated with a jet in counterflow. A jet with velocity U_j is issued into an external stream opposing the jet with velocity U_0. The jet penetrates into the external stream till it reaches stagnation point X_p. At the interface of the jet and external stream, a region of flow reversal is observed. The parameters that define the evolution of the jet are the Reynolds number of the jet Re_j and the jet to counterflow velocity ratio $\alpha = U_j/|U_0|$. Above critical values of these parameters, an instability associated with the region of flow reversal develops, leading to low frequency oscillations near the stagnation point and complex flow patterns of the jet. The instaneous snapshots of an unstable jet at $\alpha = 3.4$ are shown in figure (1.2).

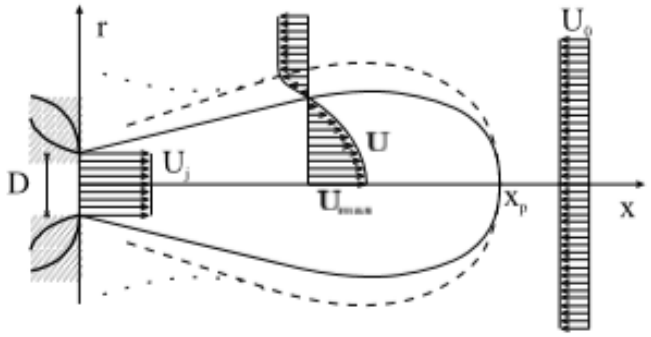

Figure 1.1. Schematic of time-averaged flowfield around a jet in counterflow, taken from Bernero [2].

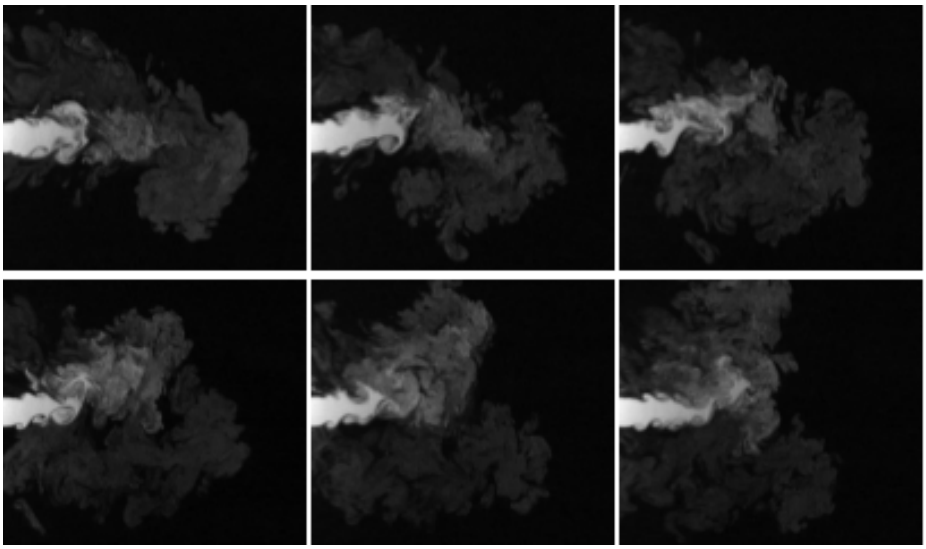

Figure 1.2. Instantaneous LIF images of an unstable jet in counterflow at $\alpha = 3.4$, taken from Bernero [2].

Understanding the behavior of the jet in counterflow is of significant interest in many applications. The marked instability in the flowfield and the oscillations of the jet introduce stirring scales and enhance jet mixing, making this configuration of jet injection suitable for combustion and chemical mixing devices. A submerged jet is often used to discharge wastewater into water bodies such as rivers and oceans. The interaction of this jet with counterflowing stream affects the local concentration of pollutants in water. Clearly, study on this configuration of jet is of environmental interest. Counterflowing jets are also used for bluff body cooling.

Other interesting applications are V/STOL aircrafts, vertical landing rockets, reverse rotating propellers and control jets used to maneuver air and under water vehicles. In these cases, the jet oscillations may lead to unpredictable thrust vectoring, making the control of the vehicle difficult. Description of the instability and the resulting oscillations may assist in devising effective control strategies.

Early research on this configuration of jet focused primarily on determining the extent to which a jet penetrates into the counterflow and investigations were conducted on time-averaged flowfield. Arendt *et al.* [1] showed that there is linear relationship (1.1) between the penatration length and the jet to counterflow velocity ratio using dimensional analysis.

$$\frac{X_p}{D} = \kappa\alpha \tag{1.1}$$

Beltaos and Rajaratnam [3] emperically derived scaling laws using experimental data from several researchers. They suggested that when the radial and axial coordinates are non-dimensionalized with the jet's axial penetration length, the radial extent of the jet penetration becomes independent of the velocity ratio. They found the value of κ to be 2.6 based on their experiments. But from their investigations, the radial extent of the jet penetration did not show clear relationship with the velocity ratio or the axial penetration length. The value of κ reported in literature varied from $2.4 - 2.9$. A summary of conducted research and the value of κ obtained by several researchers can be found in the works by Bernero [2] and Mahmoudi [7].

Sekundov [4] investigated the effects of confinement. He proposed that the counterflow can be considered as unconfined if the ratio of the counterflow width, B to the jet penetration, X_p is less than 2. Morgan *et al.* [5] identified the dependence of jet bahavior on the jet to counterflow momentum flux ratio given by (1.2). They observed that the linear relationship (1.1) holds only if $Z < 0.25$. They also showed no dependence of the jet penetration on the Reynolds number as long as it is greater than $3,000$ for the jet and $10,000$ for the counterflow.

$$Z = \left(\alpha\frac{D}{B}\right)^2 \tag{1.2}$$

A turbulent jet in confined counterflow was investigated by Sivapragasam *et al.* [6]. They analyzed the mean flowfield obtained from RANS simulations. For low momentum flux ratio cases, their results showed good agreement with previous investigations. For high momentum flux ratio, they showed that the jet penetration length reaches an asymptotic limit of about 3.57 times the confining counterflow width. They also proposed an improved similarity solution for the jet to incorporate the effects of confinement.

Several researchers attempted to study the radial extent of jet penetration. Beltaos and Rajaratnam [3] proposed that the radial extent of the jet which is reversed by the counterflow can be identified by stagnation stream surface which is the locus of points in the flowfield where the combined momentum flux of the jet and the opposing steam is zero. Based on their emperical model, they suggested that the axial coordinate, X_r and the radial coordinate, Y_r of the maximum radial extent of the jet to be about 0.75 and 0.3 times the stagnation point, X_p respectively. An accurate determination of the stagnation stream surface requires velocity data of the flowfield. However, the visulation studies conducted by K*ö*nig and Fielder [8] and by Lam and Chan [11] showed that the values of X_r and Y_r are about $0.7X_p$ and $0.4X_p$ respectively for $\alpha > 3.4$.

Hopkins and Robertson [12] conducted kinematic analysis of a two-dimensional planar jet penetration using the Helmholtz free-streamline theory. By assuming the fluids involved to be inviscid, they could obtain the solution and predicted the streamline curvature and velocity field in the jet and the counterstream using complex variables and conformal mapping. The flow patterns were analyzed by varying the jet to counterstream velocity ratio. From their experimental investigations, they observed that the flow pattern becomes unstable when $\alpha > 1.74$. And their predictions based on simplified model did not agree well with experimental findings.

Robillard and Ramamurthy [13] conducted experimental investigation of the wake generated by a planar jet issued into counterflow. They observed that the inclines towards one side till a vortex has fully grown and carried away by the counterflow. Sequentially, the jet swings to the other side and this periodic pattern is repeated. They found that the alternating vortices in the wake resemble Von Karman vortex street. The jet in their experiments was issued through a narrow slit and they found that the blockage effects the frequency of vortex shedding. They found the strouhal number of the jet to be 0.18 when the blockage is negligible.

Lam *et al.* [10] investigated the stability of a round jet in counterflow at high velocity ratio using inviscid linearized stability theory. Their results showed that counterflow increases amplification rate of the unstable modes while reducing the associated frequencies.

K*ö*nig and Fielder [8] conducted experiments and studied the jet behavior using flow visualization. They suggested that the flowfield is a combination of jet and wake, and the wake is generated by the jet. They observed a stable jet flow for velocity ratio less than 1.4. When the jet is stable, it is receptive to excitations. For the unstable case, exciting the jet did not show any influence on the flowfield. They also found that the frequency of jet oscillations has weak dependence on the velocity ratio.

Yoda and Fielder [9] studied the structure and concentration field of a round jet in counterflow using planar laser induced fluorescence (PLIF). At low velocity ratios, the flow pattern is stable, with regular vortex shedding at about $3 - 5Hz$ and the corresponding jet-based Strouhal number was found to be $0.2 - 0.3$. They observed the onset of unstable case at a velocity ratio of 1.4 and above velocity ratio of 3.4, the flow becomes unstable. The frequency of jet oscillations was found to be less than $1Hz$. The strong instability in the flowfield can be identified from the work by

Lam and Chan [14]. They found high standard deviation in the instantaneous jet penetration from the time-averaged value.

Chan and Lam [15] presented analytical expression of the jet centerline velocity decay in counterflow. Their analysis was based on langrangian formulation of the flowfield. By treating the fluid elements issued from the jet the same way as they are issued into a stagnant ambient and superimposing the advection effect from the counterflow, they could develop a model to explain velocity gradients in the flowfield. They suggested that the wavelengths of the amplified modes of instability are contracted by counterflow and are shifted to lower frequencies and the higher order azimuthal modes are contracted to approximate axisymmetric mode.

Jendoubi and Strykowski [16] investigated the stability of an inviscid axisymmetric jet in presence of external flow using spatio-temporal analysis. In their analysis, the jet mean flow was modeled by a hyperbolic tangent profile and the analysis was restricted to axisymmetric disturbances. They observed the presence of two distinct modes of instability. Mode I was found to be similar to the plane shear layer instability. Mode II is responsible for the self-excitation of the jet and is observed in the presence of strong counterflow.

Bernero and Fielder [17,18] obtained instantaneous velocity fields using particle-image-velocimetry (PIV) technique and applied proper orthogonal decomposition (POD) analysis. They investigated the unstable ($\alpha > 3.4$) and low velocity ratio cases ($\alpha \approx 1.3 - 1.4$). For both the cases, the dominant modes are the low frequency modes and correspond to the radial jet flapping and a periodic variation of the jet penetration. They made similar observation as Yoda and Fielder [9]. The most complex dynamics are observed for the low velocity ratio case. A single vortex ring is regularly shed and on reaching larger penetration length, the jet shows flapping and breaks down.

Tsunoda and Saruta [19] studied the velocity field and scalar mixing from a turbulent jet in counterflow using PIV and PLIF. They observed two distinct peaks in turbulence intensity along the jet centerline. They suggested that the first peak is related to the jet instability. The second peak is observed near the stagnation point at the maximum jet penetration location and its magnitude slightly increases with increasing velocity ratio. This observation is consistent with the computational analysis performed by Elghobashi *et al.* [20] who applied the $k - \epsilon$ RANS model.

Following the work done by Bernero and Fielder [18], Duwig and Revstedt [21] investigated the fluctuation dynamics and extracted the most energetic modes of a Re 2860 round jet in counterflow at $\alpha = 2.2$ using POD. The instantaneous snapshots were obtained from Large Eddy Simulation (LES). They found that the Strouhal number corresponding to these modes is around 0.01 and they describe a slow rotation of the jet around the centerline and low frequency axisymmetric pulsation.

Li *et al.* [22] simulated a turbulent round jet in counterflow using LES. They observed that vortex rings appear in the region near thet jet exist and convect till the stagnation point. They identified the jet oscillation in three dimensions along with rotation about the jet axis. The power spectral density (PSD) of the axial velocity fluctuations was also analyzed along the jet axis. They found that the frequency content decreases along the jet axis and the PSD rapidly decays near the stagnation point.

Jang and Mahesh [23] studied the flow around a reverse rotating propeller using LES. They investigated the massively seperated flow at a very large Reynolds number of $480,000$. They suggested that the interaction of the reverse flow with the free stream may be idealized as a round jet in counterflow. They observed that the vortex ring sheds at irregular intervals. This is due to the inherent hydrodynamic instability at high Reynolds numbers.

Gharib *et al.* [24] investigated formation and pinchoff of vortex rings. They proposed that a vortex cannot grow indefinitely as a consequence of the Kelvin-Benjamin variational principle and identified a non dimensional universal vortex formation time. Dabiri and Gharib [25] studied the vortex ring pinchoff in presence of counterflow. They showed that the vortex pinchoff can be significantly delayed in presence of counterflow.

A survey of available literature shows that the mean flow characteristics of a jet in counterflow are well understood. Most of the research effort focused on the behavior of turbulent jets. More recently, several researchers attempted to investigate the fluctuation dynamics and the coherent structures in the flowfield using POD and LES. The presence of strong instability near the stagnation point has been identified. However, several interesting aspects of the associated instability remain unclear. What is the nature and the origin of instability? Is the instability self-sustained? What are the effects of external perturbations? Why is the shedding of vortex rings observed at some velocity ratios?

Shear layer instability has been widely studied. Shear flows can be of two types: jets and wakes. Jet flows are known to behave as noise amplifiers, meaning that they amplify external disturbances while wakes support self excited modes and do not require external disturbances to sustain the instability. The presence of both these types of shear flows in the flowfield of a jet in counterflow makes the study on the associated instability interesting. A brief introduction to hydrodynamic stability theory, recent advances and its applications are presented in the next section.

1.2 Hydrodynamic stability theory

Hydrodynamic stability theory determines the reaction of a steady motion of fluid (base flow) to small disturbances. The stability of fluid flow is determined by the

growth rate of disturbances. If the disturbances grow in time, the flow is considered unstable. Conversely, the flow is considered stable if all the possible disturbances that it can be subjected to, decay in time. Hydrodynamic instability can lead to unsteadiness in the flow even when the boundary conditions are steady. The roots of this theory date to Helmholtz, Kelvin, Rayleigh and Reynolds in nineteenth century. Reynolds [26] demonstrated the instabilty in pipe flow that develops above a critical velocity. Lord Rayleigh [27] studied the breakup of a liquid jet into droplets. He found that surface tension amplifies the perturbations of certain wavelengths when the jet is perturbed sinusoidally.

The mathematical treatment of hydrodynamic stability problems was introduced by Rayleigh in 1880 [28]. He analyzed the disturbances in terms of normal modes. By decomposing the disturbances into different wavelenghts, an equation relating the wavenumber and the frequency of disturbances, known as dispersion relation can be derived. The solution determines the modes that grow/decay in time. The method of normal modes is equivalent to superimposing infinitesimal perturbations on base flow. In doing so, the linearized equations that govern the perturbations can be derived. The fluid system is considered unstable if at least one eigenvalue of the resulting linear operator exists in the right half of the complex plane. And the eigenvector associated with the most unstable eigenvalue (the most unstable mode of disturbance) is expected to dominate the form of the instability. Finding the eigenvalues and the eigenvectors is very challenging due to the large dimensions of the linear operator. The problem can be simplified if some assumptions about the base flow and the nature of disturbances are made.

Early researchers worked on the stability of viscous parallel shear flows. Orr [29, 30] and Sommerfeld [31] derived the Orr-Sommerfeld equation while attempting to investigate stability of channel flows. This equation has become essential basis of

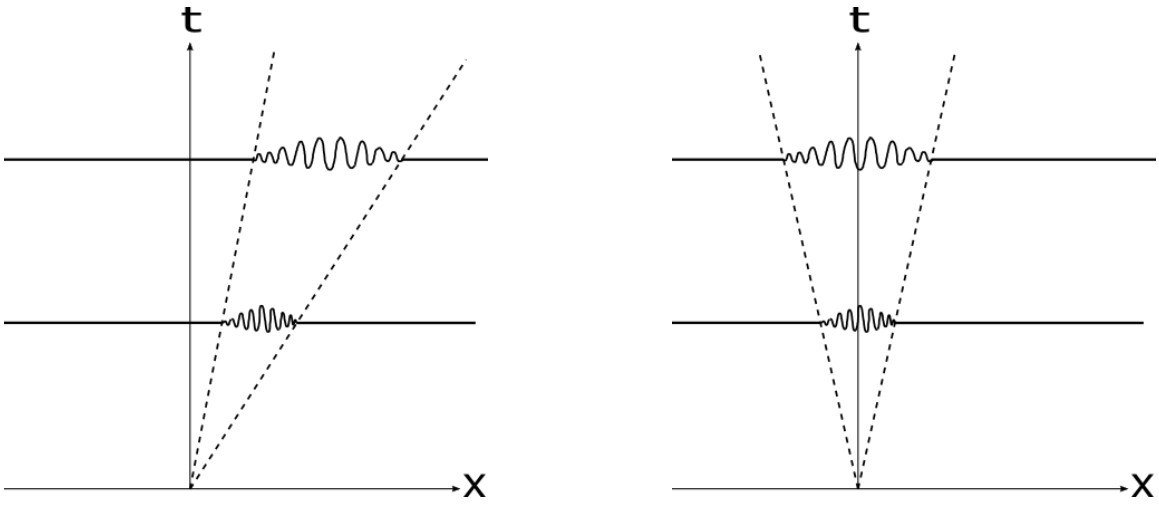

Figure 1.3. Illustration of the response to a locally introduced disturbance. (a) Convectively unstable flow, and (b) Absolutely unstable flow.

the hydrodynamic stability theory. By assuming that the disturbances grow/decay in time and oscillate in space, they posed an initial value problem whose solution determines the temporal growth of perturbations. The temporal growth analysis is not appropriate for disturbances that are generated at a fixed position in space and the spatial analog of the problem can be derived by assuming that the disturbances grow/decay in space and oscillate in time.

Following the concepts presented by Briggs [32] and Bers [33] in the study of plasma, Huerre and Monkewitz [34] introduced the notion of convective and absolute instability in the context of spatio-temporal stability analysis of fluid flows. If an initially localized impulse is amplified in at least one Galilean frame of reference but is damped in laboratory reference frame, the flow is considered to be convectively unstable. In a flow that is absolutely unstable, such impluse amplifies in laboratory frame, changing the global behavior of the flow. The difference between convective and absolute instabilities is illustrated in fig. 1.3. In convectively unstable flows, the

impulse amplifies as it convects downstream. It eventually exits the fluid domain and the flow relaxes to its unperturbed state in the absence of external forcing. In this sense, these flows are considered to be globally stable but act as noise amplifiers. An example of such a flow is a uniform density jet. In the case of an absolutely unstable flow, the impulse propagates both upstream and downstream of its initial location. A hydrodynamic feedback loop could arise if a sufficiently large region in the flow is absoultely unstable, leading to self-sustained oscillations at a well defined frequency [34–36]. These self-sustained oscillations are known as global modes of instability and the flow is globally unstable. Examples of such flows are bluff body wakes, variable density jets and jets in crossflow. Huerre and Monkewitz [37] reviewed the application of these ideas to various shear flows.

In many shear flows, the streamwise variation of the base flow affects the growth rate of disturbances. Under the WKBJ approximation [38], the absolute instability of weakly nonparallel flows can be investigated. If the wavelength of the instability is much smaller than the length scale over which the base flow changes in the streamwise direction, the local stability can be analyzed by assuming that the base flow is locally parallel. Such an analysis is called local stability analysis. However, in many absolutely unstable flows, the nonparallel effects are significant. The global stability analysis accounts for such flows by relaxing the restriction on the base flow to vary in a specific direction. It leads to a large scale eigenvalue problem. Such analyses are referred to as Bi-Global stability analysis in two-dimensions and Tri-Global stability in three-dimensions. Early investigations were limited to Bi-Global analysis. With the advances in high performance computing and numerical algorithms, researchers are now able to perform Tri-Global stability analysis of complex flows. Bagheri *et al.* [39] studied the stability of jets in crossflow and Massa [40] investigated compressible flow

over ramp injectors. Both these works attributed the self-sustained oscillations to the presence of a global instability mode.

Many researchers have identified that the eigenvalues are inadequate to completely describe the stability of fluid systems. For example, Romanov [41] showed that no matter how large the Reynolds number is, plane Couette flow never admits unstable eigenvalues. This contradicts the experimental observations which clearly show the presence of an instability beyond a critical Reynolds number. It is important to realize that the eigenvalue analysis is based on the Lypunov stability theory, where infinite time horizon is allowed for a perturbed system to retrun to equilibrium. Eigenvalues determine the asymptotic stability. However, in many fluid systems, the dynamics occur on a finite time scale. Hence, the stability analysis based on Lypunov theory is not appropriate [42].

In many shear flows, the linear operator representing the preturbation dynamics is non-normal which means that its eigenmodes are not orthogonal (interested reader should refer the book by Schmid and Henningson [43] for detailed presentation on non-normal operators). Large transient growth of perturbations may result due to the overlap of the eigenmodes [46]. Butler and Farrell [44] investigated plane channel flow and identified that the non-normality leads to large transient growth of perturbations due to streamwise advection. Cossu and Chomaz [45] showed the large amplification of initial perturbation energy in a short time due to the streamwise non-normality. This large amplification of the perturbations can take them to a regime where the linearization approximation is not valid.

As a consequence of the non-normality, the spectrum of eigenvalues of the operator is highly sensitive to perturbations. The notion of pseudospectrum was introduced by Trefethen *et al.* [47]. The pseudospectrum defines how the spectrum of eigenvalues of an operator change when the operator is perturbed with arbitrarily small perturba-

tions [48]. Non-normal systems may exibit large responses due to forcing even when the forcing frequency is far from its eigenvalue frequency. Eigenvalues are clearly inadequate in determining the stability of such systems.

Adjoint analysis of fluid systems can uncover precious information about the origin of instability and the receptivity of fluid systems to perturbations. The non-normality of a linear operator is closely related its adjoint. A non-normal operator doesn't commute with its adjoint. It can be showed that for each eigenmode of the linear operator (direct mode), there is only one non-orthogonal eigenmode of its adjoint (adjoint mode) and the corresponding eigenvalues are complex conjugate to each other [49, 50]. Chomaz [51] stated that the main source of non-normality is the change in the sign of the advection term in the adjoint equations. The base flow advection corresponds to upstream transport for the adjoint perturbations. Non-normality corresponds to the streamwise seperation of the direct and adjoint modes.

The sensitivity of the eigenvalues of the linear operator to perturbations can be obtined from the adjoint eigenmodes (see [42]). Structural sensitivity analysis involves identifying the region in the flowfield where the spectrum of eigenvalues of the linear operator is most receptive to modifications of the base flow. Strykowski and Sreenivasan [52] observed from their experiments that the vortex shedding behind a cylinder can be controlled and even suppressed by a smaller control cylinder. They idenfified the spatial regions where the placement of the control cylinder can suppress the vortex shedding. Hill [53] used linear analysis and adjoint eigenfunctions to determine the most receptive regions around the cylinder. His results are in good agreement with the experimental observations. Giannetti and Luchini [54] performed structural sensitivity analysis of flow over a cylinder. They used immersed boundary technique and located the region of the flow that is most sensitive to momentum forcing and mass injection by computing the direct and adjoint modes. Such a region

is called the wavemaker. The conditions for self-excitation develop at this region [51]. The wavemaker region can be identified by inspecting the spatial structure of the product of the direct and adjoint modes [54]. A comprehensive review on the adjoint modes and structural sensitivity analysis is presented by Luchini and Bottaro [55].

It should be noted that linear stability analyses are valid only at the onset of instability growth. Once the instability sets in, the nonlinear effects can not be neglected, especially when the non-normal effects are significant. A weakly nonlinear approach using Landau equations can be used at the beginning of instability growth [51]. Nevertheless, the linear analysis is extremely successful in predicting critical conditions for the instability growth in laminar flows [56]. Combined with structural sensitivity analysis, it sets a promising framework to investigate and control hydrodynamic instabilities [57].

1.3 Overview

The present study involves determination of the global stability of a jet in counterflow using the linear hydrodynamic stability theory. The stability of two-dimensional planar jet and a three-dimensional round jet is analyzed. Chapter 2 provides an overview of the mathematical formulation of the linear hydrodynamic stability theory. The equations governing the base flow, the linarized equations that govern the evolution of perturbations and the corresponding adjoint equations are presented. The eigenvalue problem whose solution determines the asymptotic stability is introduced. The non-normality of the Navier-Stokes operator and its effects on transient growth of perturbations is described.

Chapter 3 describes the implementation of the numerical methods required to analyze hydrodynamic stability. This includes the introduction to the embedded boundary adaptive mesh refinement strategy used to solve the Navier-Stokes

equations and the perturbation equations, the adaptive selective frequency damping method and the Newtons method used to obtain the base flow, and the matrix-free Krylov subspace method used to obtain the eigenvalues.

In chapter 4, the asymptotic stability of a planar jet and a round jet is analyzed. The computed eigen-spectrum and the critical parameters that lead to jet instability are presented.

In chapter 5, the transient energy amplification of the perturbations resulting from the non-normality effects is investigated and the optimal initial perturbations that lead to maximum energy growth are identified.

The structural sensitivity analysis of the flowfield associated with a jet in counterflow is presented in chapter 6. The regions in the flowfield, where the growth rate and the frequency of the leading eigenmode is most receptive to perturbations are located.

Chapter 7 provides a summary of the work done and the results obtained in this thesis. The future direction of this research is discussed.

CHAPTER 2

MATHEMATICAL FORMULATION

As described in the previous chapter, hydrodynamic stability theory determines the reaction of a stationary state of fluid flow to perturbations. Asymptotic stability is determined from the eigenvalue analysis. However, when the non-normal effects are significant, eigenvalue analysis is not sufficient to determine the stability of fluid flow due to the short-time amplification of the perturbations. Analysis of the adjoint equations uncovers important information about the transient growth of perturbations and the origin of the instability. It is possible to determine the receptive regions in the flowfield. The mathematical formulation of the eigenvalue analysis, transient growth of perturbations and the structural sensitivity analysis is presented in the following sections.

2.1 Base flow and the Linearized perturbation equations

The incompressible Navier-Stokes equations that govern the evolution of velocity field $\mathbf{u}$(x,t) and pressure field p(x,t) in space $\mathbf{x}$ and time t are given by

$$\nabla.\mathbf{u} = 0 \tag{2.1a}$$

$$\frac{\partial \mathbf{u}}{\partial t} + (\mathbf{u}.\nabla)\mathbf{u} = -\nabla p + \frac{1}{Re}\nabla^2\mathbf{u} \tag{2.1b}$$

$$\mathbf{u}(\mathbf{x}, 0) = \mathbf{u}_0 \tag{2.1c}$$

The above equations are non-dimensionalized by characteristic velocity scale U, length scale L and kinematic viscosity ν. Re is the Reynolds number defined as $Re = UL/\nu$.

Hydrodynamic stability theory determines the reaction of a stationary state (base flow) that satisfies the Navier-Stokes equations (2.1) to small disturbances. The base flow is essentially the time independent solution to the equations (2.1).

Equations governing the evolution of the disturbances can be derived by perturbing the base flow velocity $\mathbf{U}$ and pressure P by disturbances $\mathbf{u}^{'}$ and $p^{'}$ respectively and substituting the perturbed state

$$\mathbf{u} = \mathbf{U} + \epsilon\mathbf{u}^{'} \qquad \text{and} \qquad p = P + \epsilon p^{'} \tag{2.2}$$

into equations (2.1). In this research, only the evolution of perturbations in the linear regime is examined. This means that, the perturbations considered are small enough such that their products (terms of order ϵ^2) are neglected when compared to other terms in the equations. Under such simplification, the linearized Navier-Stokes equations that govern the evolution of the perturbations can be obtained as follows

$$\nabla.\mathbf{u}' = 0 \tag{2.3a}$$

$$\frac{\partial \mathbf{u}'}{\partial t} + (\mathbf{U}.\nabla)\mathbf{u}' + (\mathbf{u}'.\nabla)\mathbf{U} = -\nabla p' + \frac{1}{Re}\nabla^2\mathbf{u}' \tag{2.3b}$$

$$\mathbf{u}'(\mathbf{x}, 0) = \mathbf{u}'_0 \tag{2.3c}$$

It is important to specify the appropriate boundary conditions. The flow is considered to be linearly unstable if there exists at least one solution to the equations (2.3) that grows without bound as discussed in the next section.

2.2 Asymptotic stability analysis

If the equations (2.3) are projected on a divergence-free subspace and discretized in space, the following initial-value-problem (IVP) can be formulated

$$\frac{\partial \mathbf{u}^{'}}{\partial t} = \boldsymbol{A}\mathbf{u}^{'} \tag{2.4a}$$

$$\mathbf{u}^{'}(\mathbf{x}, 0) = \mathbf{u}^{'}{}_0 \tag{2.4b}$$

where $\boldsymbol{A}$ is a linear operator representing the action of the equations on the perturbation vector $\mathbf{u}^{'}$. Note that the perturbation pressure, $p^{'}$ has been omitted in equations (2.4) because, when the equations (2.3) are projected on a divergence-free subspace, the pressure and velocity are related by the solution to a Poisson equation.

The solution to the above IVP is given by

$$\mathbf{u}^{'}(t) = e^{\boldsymbol{A}t}\mathbf{u}^{'}{}_0 \tag{2.5}$$

The linear asymptotic stability of the base flow $\mathbf{U}$ depends on the eigenvalues of the operator $\boldsymbol{A}$. As time approaches infinity, the perturbations take the form of the eigenmodes, $\boldsymbol{\phi}_i$ corresponding to the least stable eigenvalues, λ_i of $\boldsymbol{A}$. We examine the following eigenvalue problem

$$\boldsymbol{A}\boldsymbol{\phi}_i = \lambda_i \boldsymbol{\phi}_i \tag{2.6}$$

The eigenvalues are generally complex. The real-part detrmines the growth rate of the perturbations and the imaginary-part determines the frequency of oscillations. If there is at least one eigenvalue with positive growth rate, the perturbations grow exponentially as given by the equation (2.5) and the perturbed fluid departs from its base flow state and never reverts to it. Such a case is considered to be asymptotically

unstable. Conversely, if all the eigenvalues of $\boldsymbol{A}$ have negative growth rate, the pertuebations decay in time and the base flow is considered to be asymptotically stable.

When the base flow is in a state of neutral stability, the growth rate of the most dominant eigenvalue of $\boldsymbol{A}$ is zero. Bifurcation analysis attempts to find the values of the non-dimensional parametrs on which the fluid flow depends, that lead to neutral stability of the flow.

2.3 Non-normality and the Adjoint equations

As discussed in section 1.2, the asymptotic stability analysis is not sufficient to descibe stability of fluids that involve finite time dynamics. In many fluid flows, the operator $\boldsymbol{A}$ is non-normal. This means that $\boldsymbol{A}$ doesn't commute with it's adjoint, $\boldsymbol{A}^*$ ($\boldsymbol{A}\boldsymbol{A}^* \neq \boldsymbol{A}^*\boldsymbol{A}$).

The adjoint operator $\boldsymbol{A}^*$ represents the action of the adjoint perturbation equations on a state vector. In obtaining the adjoint perturbation equations, it is convenient to define the inner product as

$$< \mathbf{m}, \mathbf{n} >= \int_\Omega \mathbf{m}^H \mathbf{n}\, d\nu \tag{2.7}$$

where Ω is the domain over which the equations are being solved, $\mathbf{m}$ and $\mathbf{n}$ are any vectors on Ω and $\mathbf{m}^H$ is the Hermitian (*i.e.* complex conjugate transpose) of $\mathbf{m}$.

The adjoint operator $\boldsymbol{A}^*$ satisfies the identity

$$< \boldsymbol{A}\mathbf{m}, \mathbf{n} > - < \mathbf{m}, \boldsymbol{A}^*\mathbf{n} >= b \tag{2.8}$$

where b arises from the boundary conditions and can be set to zero by selecting appropriate boundary conditions.

Using the definition of the inner product given by (2.7) and the identity (2.8), the equations governing the adjoint perturbation velocity field, $\mathbf{u}^*$ and pressure field, p^* can be obtained by integrating the equations (2.3) over the domain of investigation. The adjoint equations are given by

$$\nabla.\mathbf{u}^* = 0 \tag{2.9a}$$

$$-\frac{\partial \mathbf{u}^*}{\partial t} + (\mathbf{U}.\nabla)\mathbf{u}^* - (\nabla \mathbf{U})^T\mathbf{u}^* = -\nabla p^* + \frac{1}{Re}\nabla^2\mathbf{u}^* \tag{2.9b}$$

$$\mathbf{u}^*(\mathbf{x},\tau) = \mathbf{u}^*{}_\tau \tag{2.9c}$$

Notice the negative sign before the time derivative in equation (2.9b). This negative sign means that the adjoint equations represent the backward evolution of the perturbations. The initial condition, $\mathbf{u}^*_\tau$ for the adjoint equations is specified at an arbitrary final time of integration, τ. As observed by Chomaz [51], the base flow advection corresponds to upstream transport for the adjoint perturbations and non-normality corresponds to the streamwise seperation of the direct and adjoint modes.

The boundary conditions required to solve the adjoint equations (2.9) depend on the boundary conditions used to solve the perturbation equations (2.3). The adjoint boundary conditions are obtained by integrating the boundary conditions used for the equations (2.3). For homogeneous Dirichlet boundary conditions, the adjoint boundary conditions remain as homogeneous Dirichlet as follows

$$\mathbf{u}^*(\partial\Omega, t) = 0 \tag{2.10}$$

The Neumann outflow boundary condition (2.11) enforced on equations (2.3) requires Robin boundary condition (2.12) to be specified on the adjoint equations at the outflow boundary.

$$p^{'}\mathbf{n} - \frac{1}{Re}\nabla\mathbf{u}^{'}.\mathbf{n} = 0 \tag{2.11}$$

$$p^{*}\mathbf{n} + \frac{1}{Re}\nabla\mathbf{u}^{*}.\mathbf{n} = (\mathbf{U}.\mathbf{n})\mathbf{u}^{*} \tag{2.12}$$

However, in order to avoid the complexity involved in implementing the Robin boundary conditions, homogeneous Dirichlet boundary conditions are typically specified at the outflow boundary. The rationale is that when the outflow boundary is placed sufficiently far away, specifying Dirichlet boundary condition doesn't have a noticable effect on the evolution of perturbations. For a detailed discussion, see [58].

Similar to the problem (2.4), the following IVP can be formulated from the adjoint equations

$$-\frac{\partial\mathbf{u}^{*}}{\partial t} = \boldsymbol{A}^{*}\mathbf{u}^{*} \tag{2.13a}$$

$$\mathbf{u}^{*}(\mathbf{x},\tau) = \mathbf{u}^{*}{}_{\tau} \tag{2.13b}$$

In order to find the adjoint eigenmodes, $\boldsymbol{\phi}_i^*$, the following eigenvalue problem needs to be examined

$$\boldsymbol{A}^{*}\boldsymbol{\phi}_i^* = \lambda_i^*\boldsymbol{\phi}_i^* \tag{2.14}$$

The direct modes, $\boldsymbol{\phi}_i$ and the adjoint modes, $\boldsymbol{\phi}_i^*$ are related by

$$< \boldsymbol{A}\boldsymbol{\phi}_i,\, \boldsymbol{\phi}_i^* > = < \boldsymbol{\phi}_i,\, \boldsymbol{A}^{*}\boldsymbol{\phi}_i^* > \tag{2.15}$$

As a consequence of the non-normality of $\boldsymbol{A}$, $\boldsymbol{\phi}_i$ and $\boldsymbol{\phi}_i^*$ are non-orthogonal. Biorthogonality condition states that for each direct mode, $\boldsymbol{\phi}_i$, there is only one non-orthogonal adjoint mode, $\boldsymbol{\phi}_i^*$ and the corresponding eigenvalues, λ_i and λ_i^* respectively, are complex conjugate to each other [49, 50].

2.4 Transient growth analysis

For a fluid system to be considered stable, not only should the eigenvalues of the operator $\boldsymbol{A}$ have negative growth rate, but also the transient growth (*i.e.* the finite-time amplification) of the perturbations should be limited such that the fluid can revert to the base flow state. In transient growth analysis, we consider the energy norm of the perturbations at a given time, t as

$$E(t) = \frac{1}{2} < \mathbf{u}'(t), \mathbf{u}'(t) > \tag{2.16}$$

where, $< ., . >$ denotes the inner product operator and is defined by equation (2.7). The transient growth of perturbations over a time interval τ can be quantified by the growth of the energy norm of perturbations during that interval. The transient growth is given by

$$Q(\tau) = \frac{E(\tau)}{E(0)} = \frac{< \mathbf{u}'(\tau), \mathbf{u}'(\tau) >}{< \mathbf{u}'(0), \mathbf{u}'(0) >} \tag{2.17}$$

If homogeneous spatial boundary conditions are used, the boundary term, b in equation (2.8) becomes zero. The transient growth can then be related to the operator $\boldsymbol{A}$ and its adjoint, $\boldsymbol{A}^*$ as follows

$$\begin{aligned} Q(\tau) &= \frac{< \boldsymbol{A}\mathbf{u}'(0), \boldsymbol{A}\mathbf{u}'(0) >}{< \mathbf{u}'(0), \mathbf{u}'(0) >} \\ &= \frac{< \mathbf{u}'(0), \boldsymbol{A}^*\boldsymbol{A}\mathbf{u}'(0) >}{< \mathbf{u}'(0), \mathbf{u}'(0) >} \end{aligned} \tag{2.18}$$

It follows from the above equation that

$$< \mathbf{u}^{'}(0), \boldsymbol{A}^{*}\boldsymbol{A}\mathbf{u}^{'}(0) >=< \mathbf{u}^{'}(0), Q(\tau)\mathbf{u}^{'}(0) > \tag{2.19}$$

The non-trivial solution to the above equation leads to the following eigenvalue problem

$$\boldsymbol{A}^{*}\boldsymbol{A}\mathbf{u}^{'}(0) = Q(\tau)\mathbf{u}^{'}(0) \tag{2.20}$$

The operator $\boldsymbol{A}^{*}\boldsymbol{A}$ is symmetric with real eigenvalues and eigenmodes. The action of the operator $\boldsymbol{A}^{*}\boldsymbol{A}$ is equivalent to integrating the equations (2.4) over time interval, τ with $\mathbf{u}^{'}(0)$ as the initial condition to obtain $\mathbf{u}^{'}(\tau)$ and using this as the initial condition to integrate the equations (2.13) backwards in time over the same time interval. It can be seen that $\mathbf{u}^{'}(0)$ is the eigenmode and its transient energy growth over the time interval, τ, $Q(\tau)$ is the eigenvalue of $\boldsymbol{A}^{*}\boldsymbol{A}$.

The maximum possible transient energy growth of perturbations over the interval τ is given by

$$G(\tau) = \max(Q(\tau)) = \max_{\mathbf{u}^{'}(0)} \frac{< \mathbf{u}^{'}(\tau), \mathbf{u}^{'}(\tau) >}{< \mathbf{u}^{'}(0), \mathbf{u}^{'}(0) >} \tag{2.21}$$

The initial perturbation that leads to the maximum energy amplification over the interval τ (*i.e.* the eigenmode corresponding to $G(\tau)$) is called the optimal perturbation.

It should be noted that the optimal perturbation and its transient energy amplification are dependent on the the time interval, τ. $G_{\max}$ represents the global maximum of $G(\tau)$ over all time intervals.

The optimal perturbations and $G(\tau)$ can also be obtained from the singular value decomposition of $\boldsymbol{A}$. The optimal perturbation and the state to which it evolves

to are given by the right and left singular vectors of $\boldsymbol{A}$ respectively. And $G(\tau)$ is given by the leading singular value.

2.5 Structural sensitivity

Structural sensitivity analysis involves identifying the region in the flowfield where small perturbations will have largest impact on the instability. Such a region in the flowfield can be thought of as the origin of instability and is termed as wavemaker. The conditions for self-excitation of the disturbances develop through a feedback mechanism at the wavemaker region.

The direct modes determine the response of the flow to the pertrubations and the adjoint modes determine the sensitivity. The overlap of direct and adjoint modes determines the region where the response is most sensitive. In determining the wavemaker, both the direct and the adjoint modes need to be considered.

As determined by Giannetti and Luchini [54], the structural sensitivity map of the flowfield can be obtained by considering the dyadic product of the adjoint and the global modes. The structutal sensitivity tensor is given by $\zeta_{ij} = \boldsymbol{\phi}_i \boldsymbol{\phi}_j^*$. The wavemaker region is determined by the Forbenius norm of the sensitivity tensor and is given by

$$\delta\lambda = \frac{\|\boldsymbol{\phi}\|\|\boldsymbol{\phi}^*\|}{|<\boldsymbol{\phi}, \boldsymbol{\phi}^*>|} \tag{2.22}$$

2.6 Chapter summary

The mathematical formulation of the linear hydrodynamic stability analysis is discussed in this chapter. The stability of a fluid flow is determined by its ability to revert to its stationary state when it is subjected to disturbances. The equations

governing the stationary state and the evolution of small perturbations are presented. The discretized equations can be represented by a linear operator. The disturbances may undergo finite-time amplification as a consequence of the non-normality of the linear operator. While the asymptotic growth of the disturbances is determined by the eigenvalues of the linear operator, their transient growth is given by the singular value decomposition of the operator. The eigenmodes of the adjoint operator can reveal the origin of instability (*i.e.* the wavemaker region). The overlap of the direct and adjoint modes determine the structural sensitivity of the flowfield.

CHAPTER 3

NUMERICAL IMPLEMENTATION

Performing linear stability analysis of fluid flows involves determining the base flow and its reaction to small disturbances. Base flow is the steady state solution to the Navier-Stokes equations and its reaction to disturbances is determined by the solution to eigenvalue problem as discussed in the previous chapter. This presents two major challenges. When the fluid is absolutely unstable, techniques like Newton iterations or selective frequency damping (SFD) need to be implemented. And, the dimensions of the operators whose eigenvalues determine the stability are prohibitively large to store in memory. Matrix-free iterative methods are required to determine the eigenvalues. The numerical methods used to obtain the solutions to the equations presented in chapter 2 and the algorithms used to obtain the base flow and to solve the large-scale eigenvalue problem are described in this chapter.

3.1 Flow solver

The incompressible Navier-Stokes equations (2.1) are numerically solved using a second-order finite volume scheme. The solver is developed in C++ based on the CHOMBO library [59]. The cartesian mesh used to spatially discretize the equations is dynamically refined based on the computed solution. Such a technique is called adaptive mesh refinement (AMR). The patch-based refinement strategy is implemented. The surfaces of the solid bodies are embedded in the computational mesh using the cut-cell approach. The solid boundaries are represented by a set of implicit geometric functions and the geometric information (volume fractions, area fractions,

cell centers, etc.) is stored as a graph. The fluxes at the solid boundaries are evaluated using the immersed boundary method.

The flow solver used in this research follows the algorithm described by Trebotich and Graves [60]. The equations (2.1) are solved using predictor-corrector formulation. The divergence-free constraint is enforced by the solution to Poisson equation based on Hodge decomposition. The algorithm uses the marker and cell (MAC) formulation to compute the cell-centered projection and the face-centered gradients. At the intersection of the coarse and fine patches of mesh, the solution is smoothed by the averaging operators. A semi-implicit scheme is implemented. The convective fluxes are calculated using second-order upwinding scheme and are treated explicitly. And, the velocity is updated by solving the Helmholtz equation resulting from the viscous terms implicitly. The pressure field is obtained by solving the Poisson equation that is obtained from Hodge decomposition. The laplacian operator is discretized using second-order central differencing. The overall scheme is second-order accurate in space.

The explicit treatment of the convective fluxes imposes restriction on the time step size due to the CFL condition. In cut-cell approaches, this restriction can be particularly severe. This issue is avoided using volume-weighted scheme during the explicit advance of the solution. The convergence of the linear solvers used for the Helmholtz and Poisson solves is accelerated using multigrid method coupled with Gauss-Seidel relaxations. Grid coarsening is performed both within each level of refined mesh and accross levels. Bi-conjugate gradient method is used as the bottom solver.

The algorithm can be modified to solve the linear perturbation equations (2.3) and the adjoint equations (2.9) as described by Liu *et al.* [61] and by Barkley *et al.* [58]. The terms $(\mathbf{u}'.\nabla)\mathbf{U}$ and $(\nabla\mathbf{U})^T\mathbf{u}^*$ in eq. (2.3) and eq. (2.9) respectively,

effect the solution procedure used to solve the Navier-Stokes equations in two ways: (i) they need to be considered during the extrapolation of cell-centerd solution to faces to maintain stable second order flux computation (see [62, 63]), and (ii) the source term in the Helmholtz equation is modified.

The temporal discretization is done using either the first order backward Euler scheme to obtain time-independent base flow or a modified second order Runge-Kutta scheme [64] for the linearized perturbation and the adjoint equations.

3.2 Steady state solution (Base flow)

Performing stability analysis requires the steady state solution to the Navier-Stokes equations. When the flow is globally unstable, it is impossible to time-march to steady state. Finding the base flow in such a case is challenging. This research implements the Newton's iteration method and a feedback control-based selective frequency damping (SFD) method to obtain the base flow. These methods are described in the following sections.

3.2.1 Newton's method

The incompressible Navier-Stokes equations (2.1) can be schematically represented as

$$\frac{\partial \mathbf{u}}{\partial t} = N(\mathbf{u}) + L(\mathbf{u}) \tag{3.1}$$

where L represents the viscous term and N represents the effect of non-linear convective term and the divergence-free constraint enforced through the solution to the pressure-Poisson equation based on Hodge decomposition.

The roots of the operator on the right hand side of the equation (3.1) are found by Newton iteration:

$$\begin{aligned}(N_{\mathbf{u}} + L)\delta\mathbf{u} &= (N + L)\mathbf{u} \\ \mathbf{u} &:= \mathbf{u} - \delta\mathbf{u}\end{aligned} \tag{3.2}$$

where $N_{\mathbf{u}}$ represents the Jacobian of N evaluated at $\mathbf{u}$.

It is very challenging to find the inverse of the Jacobian using direct methods. Also, the equation (3.2) is ill-conditioned. This research implements the matrix-free time-stepper approach introduced by Tuckerman and Barkley [65].

By using the operator $(I - \Delta tL)^{-1}$ as a preconditioner on the equation (3.2), the following equation can be obtained

$$\begin{aligned}(I - \Delta tL)^{-1}(N_{\mathbf{u}} + L)\delta\mathbf{u} &= (I - \Delta tL)^{-1}(N + L)\mathbf{u} \\ (I - \Delta tL)^{-1}[I + \Delta tN_{\mathbf{u}} - (I - \Delta tL)]\delta\mathbf{u} &= (I - \Delta tL)^{-1}[I + \Delta tN - (I - \Delta tL)]\mathbf{u} \\ [(I - \Delta tL)^{-1}(I + \Delta tN_{\mathbf{u}}) - I]\delta\mathbf{u} &= [(I - \Delta tL)^{-1}(I + \Delta tN) - I]\mathbf{u}\end{aligned} \tag{3.3}$$

where I represents the indentity operator.

The solution obtained from the flow solver implementing the first order semi-implicit time marching scheme can be represented as

$$\mathbf{u}(t + \Delta t) = (I - \Delta tL)^{-1}(I + \Delta tN)\mathbf{u}(t) \tag{3.4}$$

By comparing the equation (3.3) with (3.4), we notice that the right hand side of (3.3) is the difference between two time steps and the left hand side is the difference obtained from the linearized Navier-Stokes solver. Equation (3.3) is solved using Bi-conjugate gradient method provided by the CHOMBO software package [66]. However, quadratic convergence of this method is achieved only when the iterations are started with an initial guess that is close enough to the base flow.

3.2.2 Selective frequency damping (SFD)

The Selective frequency damping method was introduced by Åkervik *et al.* [67] as an alternative to the Newton's method. This method is derived from feedback control technique. The original system of equations, given by

$$\frac{\partial \mathbf{u}}{\partial t} = F(\mathbf{u}) \tag{3.5}$$

are modified in two ways.

The fluid state is augmented by adding a linear forcing term that is proportional to the instantaneous state and the time-filtered state. And the second modification involves adding the differential form of the low-pass time filter to the original system. The modified system of equations is

$$\frac{\partial \mathbf{u}}{\partial t} = F(\mathbf{u}) - \chi(\mathbf{u} - \bar{\mathbf{u}}) \tag{3.6a}$$

$$\frac{\partial \bar{\mathbf{u}}}{\partial t} = \frac{\mathbf{u} - \bar{\mathbf{u}}}{\Delta} \tag{3.6b}$$

In equation (3.6), χ is called as control coefficient and Δ is called as damping coefficient. At the steady state, $\mathbf{u} = \bar{\mathbf{u}}$ and hence, the steady state solution of the equations (3.6) is also solution of the original system of equations (3.5). The flow solver can be easily modified to solve the augmented system of equations (3.6) by following the encapsulated algorithm formulated by Jordi *et al.* [68]. The system of equations (3.6) can be formulated as two subproblems using first order operator splitting method as follows

$$\begin{aligned} \dot{\mathbf{u}} &= F(\mathbf{u}), \\ \dot{\bar{\mathbf{u}}} &= 0 \end{aligned} \tag{3.7a}$$

and

$$\begin{aligned} \dot{\mathbf{u}} &= -\chi(\mathbf{u} - \bar{\mathbf{u}}), \\ \dot{\bar{\mathbf{u}}} &= \frac{\mathbf{u} - \bar{\mathbf{u}}}{\Delta} \end{aligned} \tag{3.7b}$$

The first subproblem (3.7a) is the originial system of equations, whose solution, $\mathbf{u}^*$ at the time step $(n+1)$is obtained from the flow solver without any modifications. The solution to (3.7a) is used as the initial condition to solve the second subproblem (3.7b), whose solution is given by

$$\begin{pmatrix} \mathbf{u}^{n+1} \\ \bar{\mathbf{u}}^{n+1} \end{pmatrix} = S \begin{pmatrix} \mathbf{u}^{*} \\ \bar{\mathbf{u}}^{n} \end{pmatrix} \tag{3.8}$$

where S is given by

$$S = \frac{1}{1+\chi\Delta} \begin{pmatrix} I + \chi\Delta I e^{-(\chi+\frac{1}{\Delta})\Delta t} & \chi\Delta I[1 - e^{-(\chi+\frac{1}{\Delta})}] \\ I - I e^{-(\chi+\frac{1}{\Delta})\Delta t} & \chi\Delta I + I e^{-(\chi+\frac{1}{\Delta})\Delta t} \end{pmatrix} \tag{3.9}$$

The advantage of SFD method over Newton's method is that the convergence is independent of the initial guess. However, the convergence is strongly affected by χ and Δ. They should be chosen such that all the unstable modes are be damped. When the system has both high and low unstable frequencies, a multi-damper approach [40] can be used to stabilize the system.

This research implements the adaptive SFD scheme introduced by Jordi *et al.* [69]. This method involves obtaining an approximate base flow by choosing initial values for χ and Δ. These parameters are then adapted based on a one-dimensional model problem considered as follows

$$u^{n+1} = \lambda_D u^n \tag{3.10}$$

where λ_D is the estimated eigenvalue that needs to be damped by SFD.

The application of SFD scheme to the model problem (3.10) can be written as

$$\begin{aligned}\begin{pmatrix} u^{n+1} \\ \bar{u}^{n+1} \end{pmatrix} &= S \begin{pmatrix} \lambda_D & 0 \\ 0 & 1 \end{pmatrix} \begin{pmatrix} u^{n} \\ \bar{u}^{n} \end{pmatrix} \\ &= M \begin{pmatrix} u^{n} \\ \bar{u}^{n} \end{pmatrix}\end{aligned} \tag{3.11}$$

The convergence of the problem depends on eigenvalues of M which in turn depend on λ_D, χ and Δ. Fastest convergence is achieved when the dominant eigenvalue of M is smallest. An optimization problem can be formulated to find χ and Δ for a given λ_D that minimize the leading eigenvalue of M. This research uses the differential evolution method provided by the SciPy package [70] to find the optimal values.

However, from the conducted numerical experiments, it is found that no set of χ and Δ is able to damp very low frequency modes and the stationary modes. This finding is consistent with the work done by Cunha *et al.* [71] who used dynamic mode decomposition (DMD) to find the optimal SFD parameters. In such a case, base flow is obtained using Newton's method.

3.3 Eigenvalue solver

Due to the large memeory requirements to store the linearized Navier-Stokes operator, $\boldsymbol{A}$, the direct methods to solve the eigenvalue problems (2.6), (2.14) and (2.20). The search for global modes is carried out using the block Krylov-Schur (BKS) method implemented in Anasazi package [72] which is part of the Trilinos library. When the block size is set to one, this method is mathematically equivalent to the widely used implicitly restarted Arnoldi method (IRAM) [73] but it offers two advantages [74]:

(i) it is easier to deflate the converged Ritz vectors and (ii) the potential forward instability of the QR algorithm is avoided. Better convergence of the Krylov-Schur method is observed when compared to IRAM [75].

This method is based on the Krylov subspace projection technique. The basic principle is to find the best approximations to the eigenvectors of the operator in a subspace of much smaller dimension. The Krylov subspace of dimension m associated with an operator $\boldsymbol{B}$ and initial vector $\mathbf{u}_0$ is of the form

$$\mathcal{K}_m \equiv \text{span}\left\{\mathbf{u}_0,\ \boldsymbol{B}\mathbf{u}_0,\ \boldsymbol{B}^2\mathbf{u}_0,\ \ldots \boldsymbol{B}^{m-1}\mathbf{u}_0\right\} \tag{3.12}$$

If $\boldsymbol{B}$ represents the exponential of the linear Navier-Stokes operator, $\boldsymbol{A}$ ($\boldsymbol{B} \equiv e^{\boldsymbol{A}\Delta t}$), then the Krylov subspace (3.12) is spanned by solution snapshots that are seperated by time interval Δt. The subspace is formed by starting with an initial non-zero vector $\mathbf{u}_0$ and repeatedly advancing the linear Navier-Stokes solver by Δt till the dimension m is reached. The time interval Δt should be chosen such that Nyquist criterion is satisfied. The snapshots are orthonormalized using the classic Gram-Schmidt procedure and the eigen-decomposition of the subspace projected operator is obtained using QR-algorithm.

The eigenmodes of the operator $\boldsymbol{B}$ and $\boldsymbol{A}$ are the same. The eigenvalues λ_i of $\boldsymbol{A}$ can be recovered from the eigenvalues σ_i of $\boldsymbol{B}$ using the transformation

$$\lambda_i = \frac{\ln(\sigma_i)}{\Delta t} \tag{3.13}$$

The procedure for finding the adjoint modes and the optimal initial perturbations is identical. In the case of adjoint analysis, $\boldsymbol{B} \equiv e^{\boldsymbol{A}^*\Delta t}$. *i.e.* the subspace is spanned by the snapshots obtained from the adjoint solver. In transient growth analysis, $\boldsymbol{B} \equiv \boldsymbol{A}^*\boldsymbol{A}$. This is equivalent to integrating the equations (2.4) over time

interval, τ with $\mathbf{u}'(0)$ as the initial condition to obtain $\mathbf{u}'(\tau)$ and using this as the initial condition to integrate the equations (2.13) backwards in time over the same time interval.

3.4 Validation

3.4.1 Analysis of two-dimensional flow over cylinder

Bi-Global stability analysis of flow over cylinder is conducted to test the implementation of the numerical methods described in the previous sections. The domain of investigation is shown in figure (3.1). The simulations are performed on the domain $[-50, -25]$ x $[50, 25]$. A cylinder with diameter 1 unit is placed at $(0, 0)$.

The left, top and bottom boundaries of the domain are modeled as farfield boundaries, where Dirichlet boundary conditions on velocity are enforced. During the base flow computation, the velocity is set to $(1, 0)$ and the right boundary of the domain is modeled as outflow boundary. At the cylinder surface, no-slip boundary

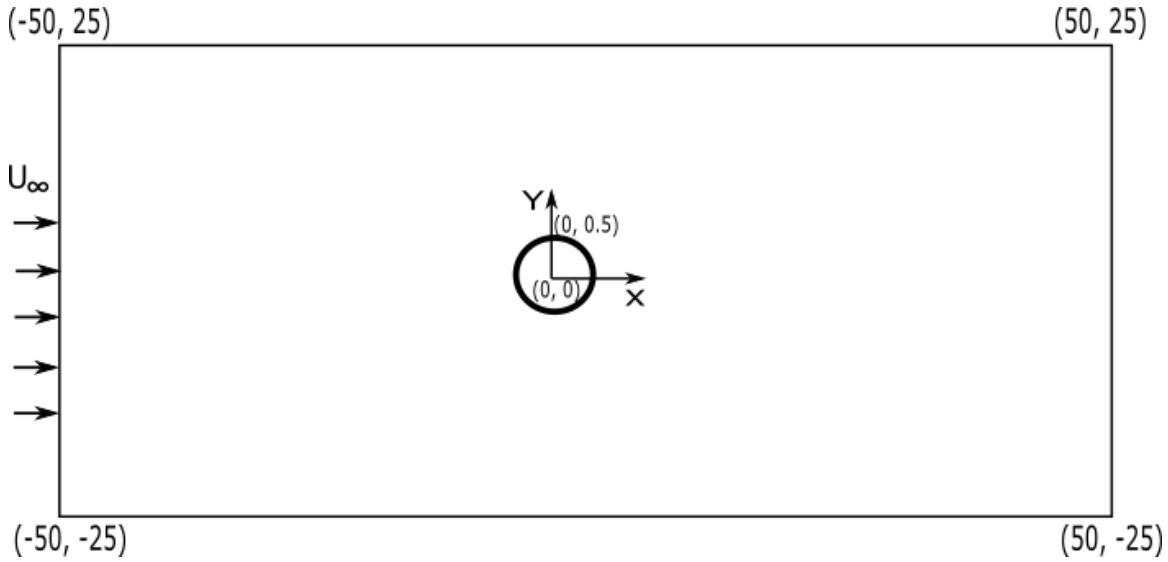

Figure 3.1. Schematic description of the domain.

conditions are used. The velocity of perturbations on all the boundaries during both direct and adjoint solves are set to $(0, 0)$.

The domain is discretized with a base mesh of resolution 512 x 512. One level of finer mesh with a refinement ratio of 2 is added at the regions with vorticity greater

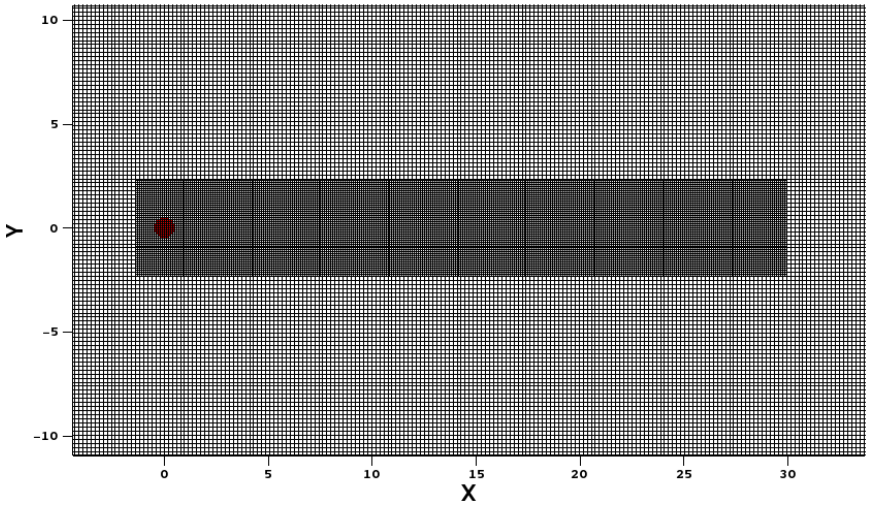

(a) One level of refinement adapted to base flow vorticity for $Re = 100$

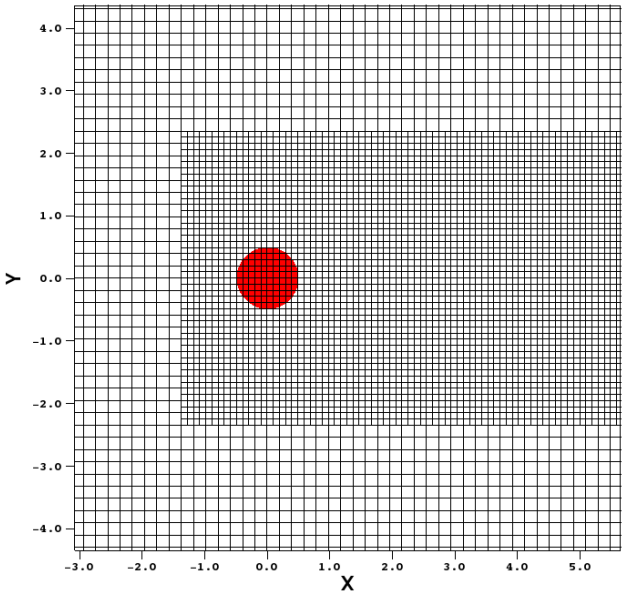

(b) Embedded boundary representation of cylinder

Figure 3.2. Discretized computational domain.

than 1 unit. The refined mesh and the embedded boundary representation of the cylinder is shown in figure (3.2).

Stability analysis is performed at $Re = 50$ and at $Re = 100$. Base flow is computed using the adaptive SFD method. The initial values of the parameters (χ_{init}, Δ_{init}) are chosen to be (1, 2). The optimal parameters, (χ_{opt}, Δ_{opt}) are found to be (0.382, 2.6904) for the $Re = 50$ case and (0.4416, 3.2173) for $Re = 100$ case. The SFD iterations are stopped when $||\mathbf{u} - \bar{\mathbf{u}}||_{\text{inf}} < 10^{-4}$. The vorticity contours of the base flow for $Re = 50$ and $Re = 100$ are shown in figure (3.3).

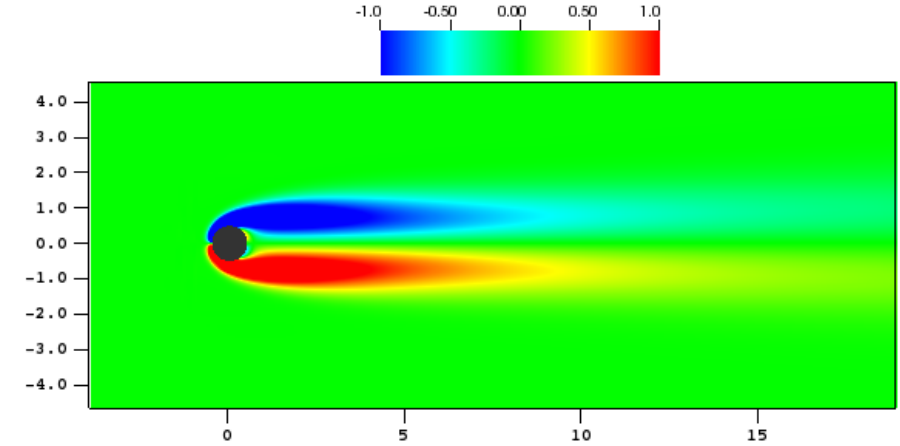

(a) $Re = 50$

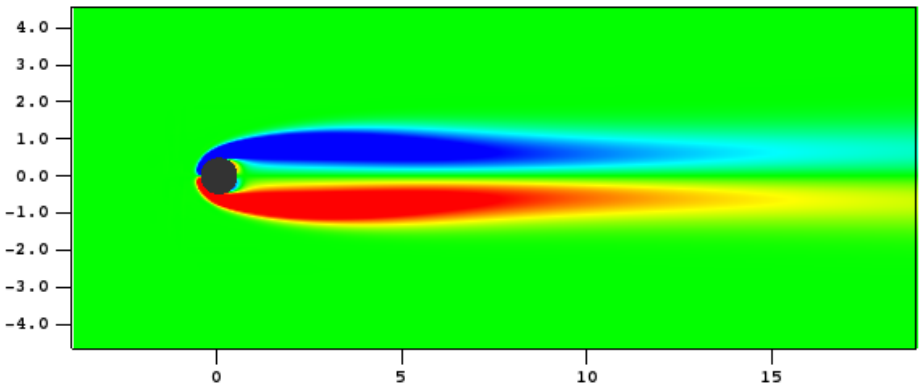

(b) $Re = 100$

Figure 3.3. Base flow vorticity.

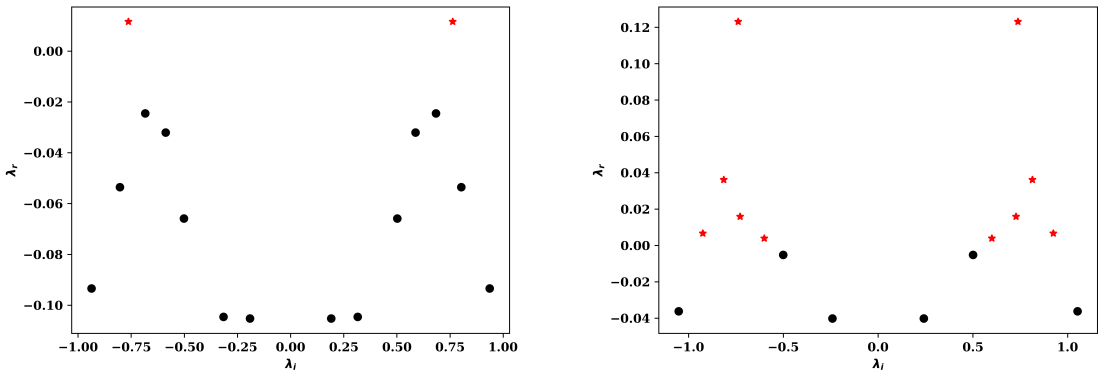

(a) $Re = 50$ (b) $Re = 100$

Figure 3.4. Spectrum of eigenvalues. X-axis shows the imaginary part and Y-axis shows the real part. Eigenvalues corresponding to the stable modes are shown in black while the ones corresponding to unstable modes are shown in red.

The base flows shown in fig. (3.3) are used to compute the direct and adjoint modes. 1 block with a size of 41 resulting in a subspace dimension of 42 is used to search for the global modes. The integration time between the snapshots is set to be equal to 1. The residual corresponding to the leading 16 modes reached $< 10^{-4}$ within 120 iterations. The most dominant eigenvalue of the linear operator is found to be $0.0131 \pm i\,0.7403$ for $Re = 50$ and $0.1253 \pm i\,0.732$ for $Re = 100$. This is in good agreement with the value reported in literature [54, 76]. Figure 3.4 shows the computed spectrum of eigenvalues. The vorticity contours of the real and imaginary part of the most unstable direct mode is shown is figures 3.5 and 3.6.

The eigenvalue corresponding to the leading adjoint mode is found to be $0.0131 \pm i\,0.7381$ for $Re = 50$ and $0.1246 \pm i\,0.722$ for $Re = 100$. The figures 3.7 and 3.8 show the vorticity contours of the real and imaginary part of the most unstable adjoint mode. The discontinuous features in the figures is due to the coarse mesh and the lack of interpolation to cell centers from faces by the visualization software.

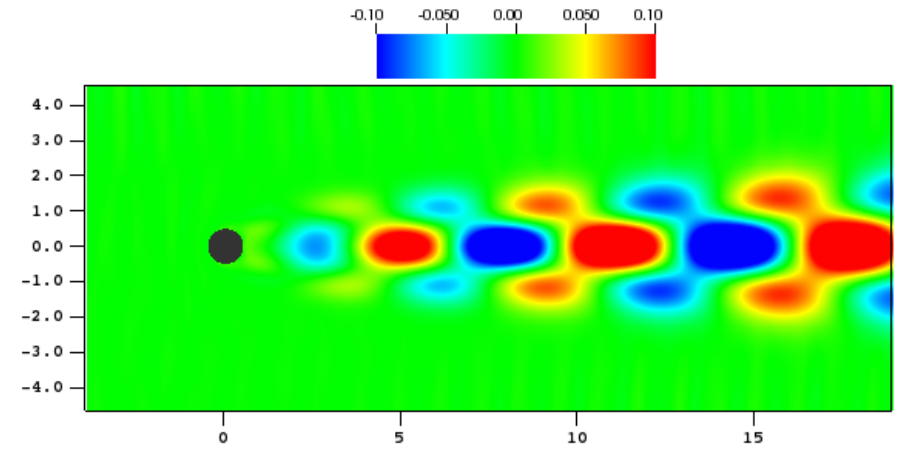

(a) Real part

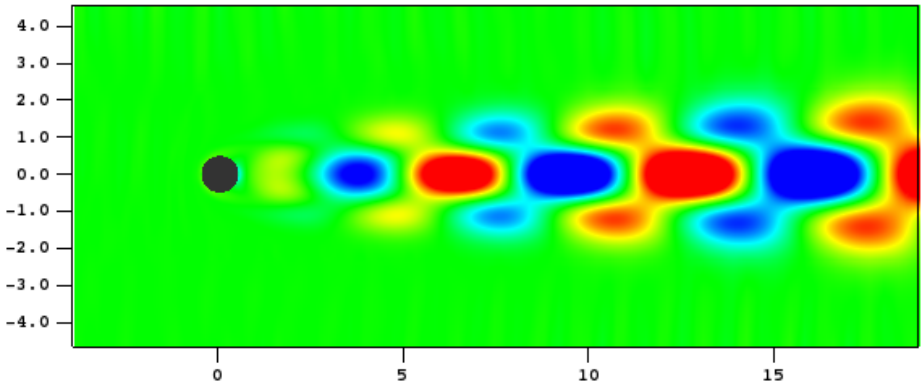

(b) Imaginary part

Figure 3.5. Vorticity contour of the dominant direct mode for $Re = 50$.

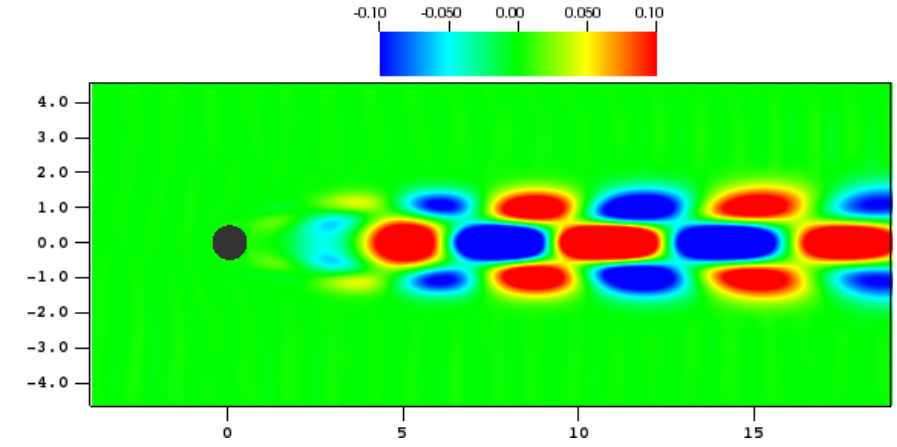

(a) Real part

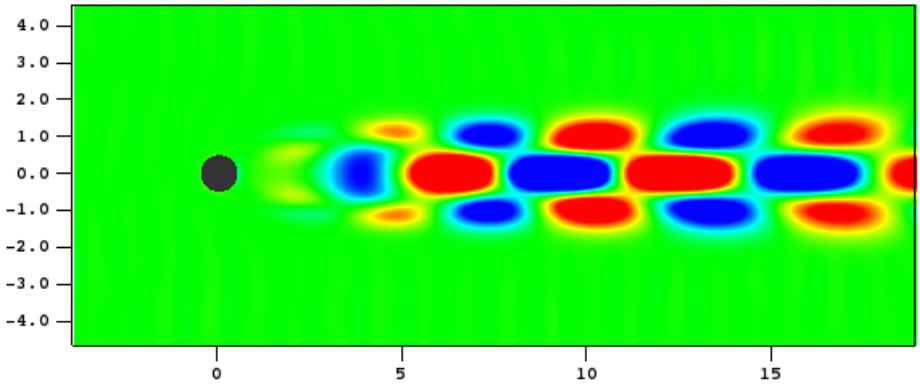

(b) Imaginary part

Figure 3.6. Vorticity contour of the dominant direct mode for $Re = 100$.

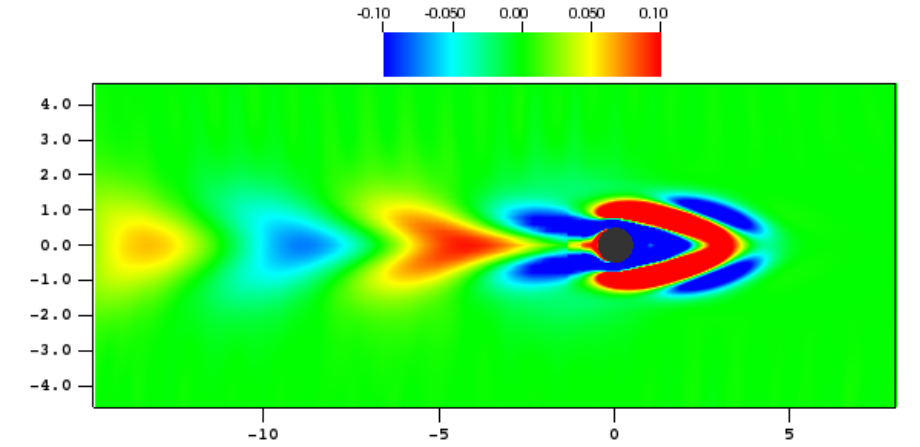

(a) Real part

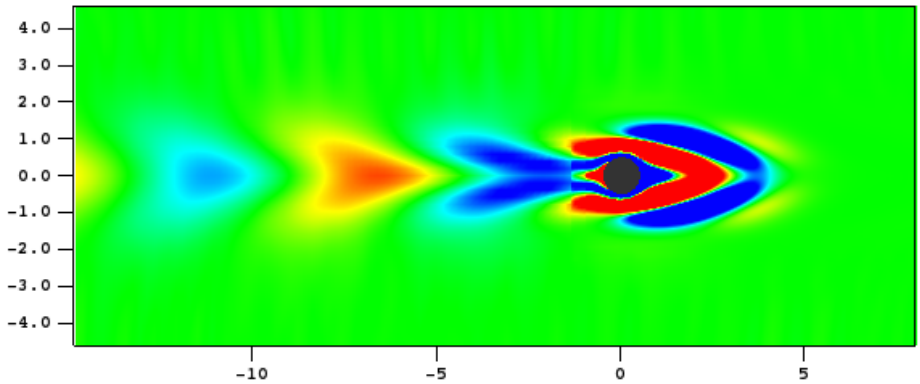

(b) Imaginary part

Figure 3.7. Vorticity contour of the dominant adjoint mode for $Re = 50$.

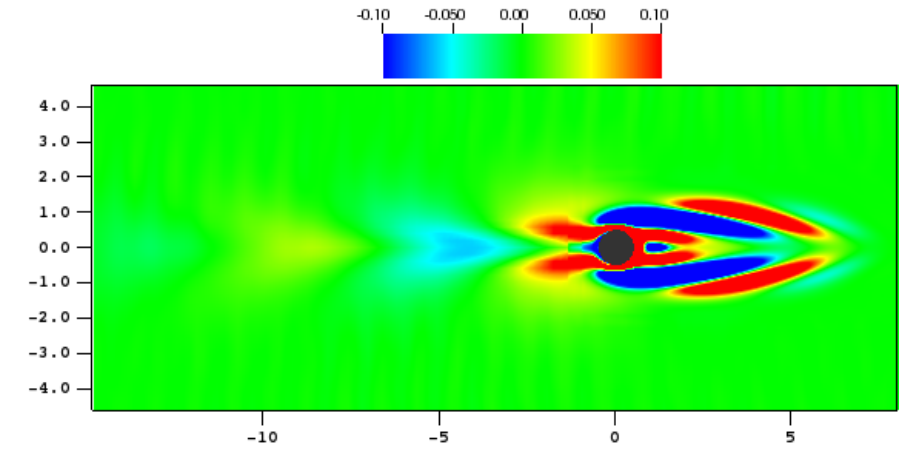

(a) Real part

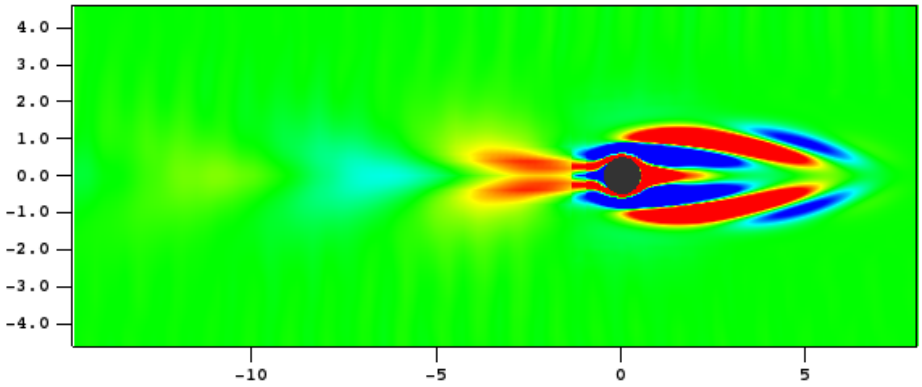

(b) Imaginary part

Figure 3.8. Vorticity contour of the dominant adjoint mode for $Re = 100$.

3.5 Chapter summary

The numerical methods used in this research are described in this chapter. The incompressible Navier-stokes equations, the linearized perturbation equations and the adjoint equations are numerically solved using the Embedded boundary finite volume method. The accuracy of the solution is locally improved using the adaptive mesh refinement strategy.

When the flow is globally unstable, it is impossible to find the base flow by marching in time. This research implements adaptive selective frequency technique to find the base flow state. However, from the conducted numerical experiments it is found that the SFD technique is unable to damp very low frequency and stationary unstable modes. In such a case, base flow is found using Newton's method. This method is implemented using matrix-free time-stepper approach.

The search for global modes of instability is carried out using block Krylov-Schur method. By forming a subspace that is spanned by the solution snapshots, substantial information about the dominant modes of the operator is obtained. The eigenmodes of the subspace are equal to the eigenmodes of the operator that is projected onto the subspace.

Bi-Global stability of flow over a cylinder is computed at $\mathrm{Re} = 50$ and $\mathrm{Re} = 100$ to validate the implementation of the described methods. The computed eigenvalues are in close agreement with published literature. The spectrum of eigenvalues and the dominant direct and adjoint modes are visualized.

CHAPTER 4

ASYMPTOTIC STABILITY ANALYSIS

The numerical methods described in the previous chapter are applied to study the stability of a jet in counterflow. The asymptotic stability of a two-dimensional planar jet and a round jet is calculated. The stability of the jet depends on its Reynolds number,

$$Re_{jet} \equiv \frac{U_{jet} D}{\nu} \tag{4.1}$$

and the jet to counteflow velocity ratio,

$$\alpha \equiv \frac{U_{jet}}{U_0} \tag{4.2}$$

where U_{jet} is the jet centerline velocity and U_0 is the counterflow velocity.

The base flow states for different values of jet based Reynolds number and jet to counterflow velocity ratio are obtained. The eigenvalues are computed using the block Krylov-Schur method and the most dominant direct modes are visualized. The computational setup, base flow sates and the results from the eigenvalue analysis are presented in the following sections.

4.1 Bi-Global stability analysis of a planar jet in counterflow

4.1.1 Problem setup

The computational setup used for the Bi-Global stability analysis of planar jet in counterflow is schematically described in figure (4.1). The simulations are performed on the domain $[-32, -32]$ x $[32, 32]$. The jet inlet is placed on the left boundary and is issued through a channel with width 1 unit and length 32 units. The thickness of

the channel walls is taken to be 0.2 times the channel width, D (not represented in figure (4.1)). The counterflow enters the domain from the right boundary.

During the base flow computation, the right, top and the bottom boundaries of the domain are modeled as farfield boundaries, where Dirichlet boundary conditions on velocity are enforced. The velocity is set to $(-U_0, 0)$, where U_0 represents the counterflow velocity. At the jet inlet on the left boundary, fully-developed parabolic profile with centerline velocity 1.5 is enforced on the x-velocity and the y-velocity is set to 0. At the left boundary outside the jet inlet, outflow boundary conditions are enforced. The channel walls are treated as no-slip boundaries. During the eigenvalue computation, the velocity of perturbations on all the boundaries is set to $(0, 0)$.

The domain is discretized with a base mesh of resolution 256 x 256 as shown in figure (4.2). The channel walls are embedded into the cartesian mesh. Finer levels of mesh with a refinement ratio of 2 are added at the regions where base flow vorticity, ω is greater than $0.5U_0/D$. A buffer region of two cells is added around each tagged

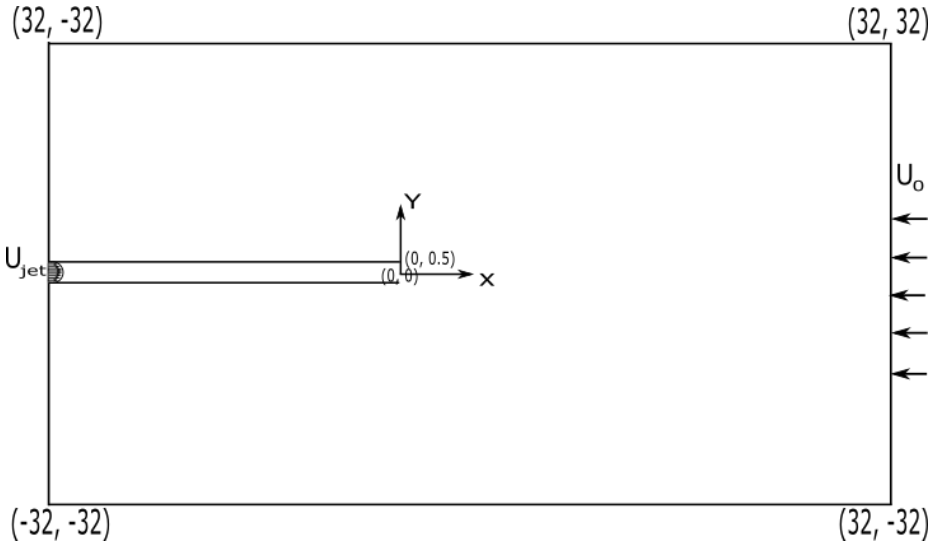

Figure 4.1. Schematic description of the computational setup used for stability analysis of planar jet in counterflow.

cell for all levels of refinement. Grid convergence study is preformed by computing the eignvalues on meshes different levels of refinement. Based on the grid convergence study, three levels of refinement are found to be sufficient. Figure (4.3) shows mesh adapted to the base flow vorticity for the case of a $Re = 50$ jet at velocity ratio of 1.7.

4.1.2 Stability of the jet at $Re = 50$

The stability of the jet at $Re = 50$ is analyzed with an increasing velocity ratio in this section. The jet is issued through the channels with a parabolic profile and

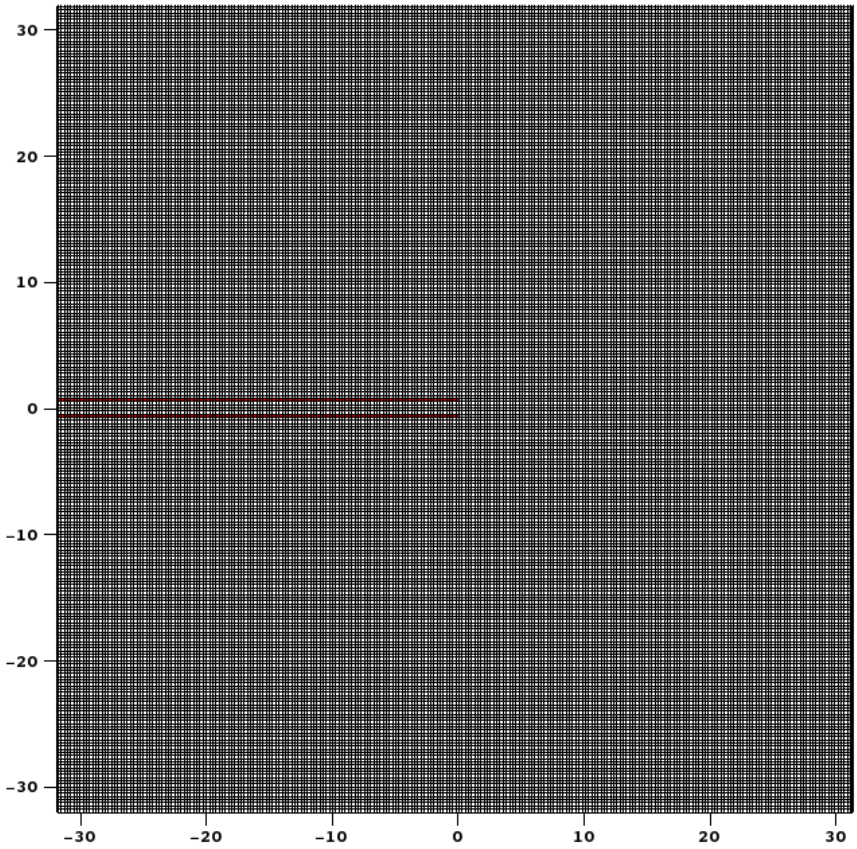

Figure 4.2. Base mesh used to discretize the domain. Channel walls (shown in red) are modeled as embedded boundaries.

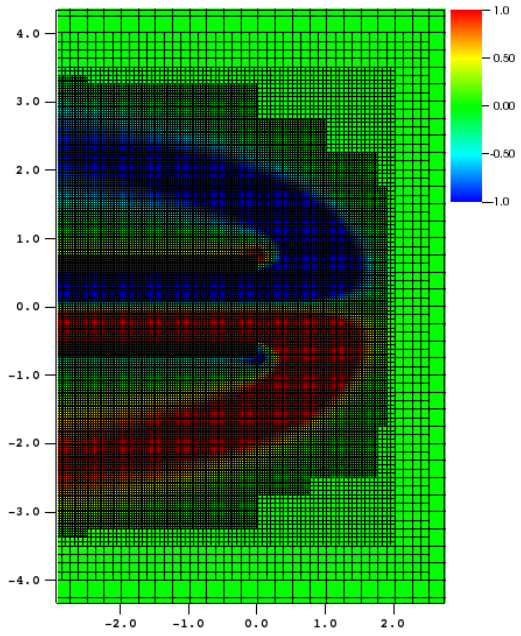

Figure 4.3. Three levels of mesh refinement added to the base flow. The mesh is adapted to the regions in the flowfield with $\omega > 0.5U_0/D$. The case of jet at $Re = 50$ and $\alpha = 1.7$ is shown here.

the centerline velocity is fixed at 1.5 units. The jet to counterflow velocity ratio is increased by reducing the counterflow velocity.

The base flow solution is obtained using the adaptive selective frequency damping method. The SFD iterations are stopped when $||\mathbf{u} - \bar{\mathbf{u}}||_{\text{inf}} < 10^{-4}$. However, for the case of $\alpha = 2.0$, the adaptive SFD method failed to provide the parameters that could damp the unstable mode. For this case, the SFD method is run till $||\mathbf{u} - \bar{\mathbf{u}}||_{\text{inf}}$ reaches $\approx 3\text{x}10^{-2}$. This partially converged solution is provided as initial guess to the Newton's method. The base flow solution is obtained when the L_2 norm of the step size is reduced to $< 10^{-6}$. Figure (4.4) shows the computed base flow solution. The base flow is specularly symmetric as expected. The jet penetration length into the counterflow increases with α. At $\alpha = 1.3$, the penetration length is around $0.7D$ and at $\alpha = 2.0$, it is around $4.3D$.

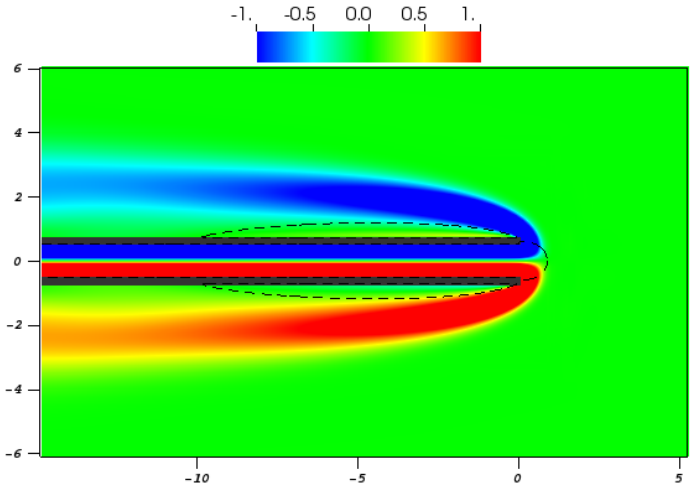

(a) $\alpha = 1.3$

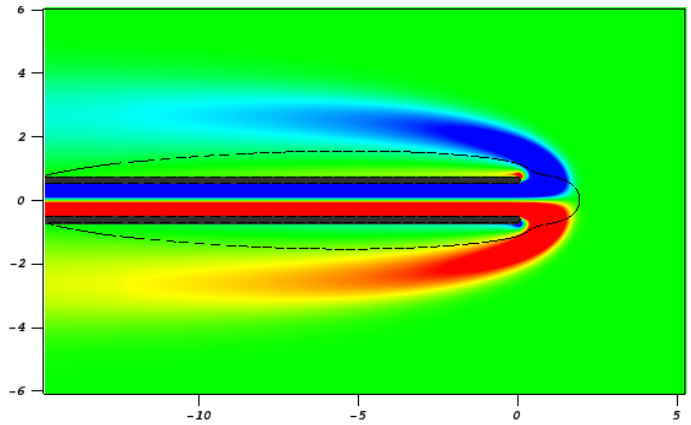

(b) $\alpha = 1.7$

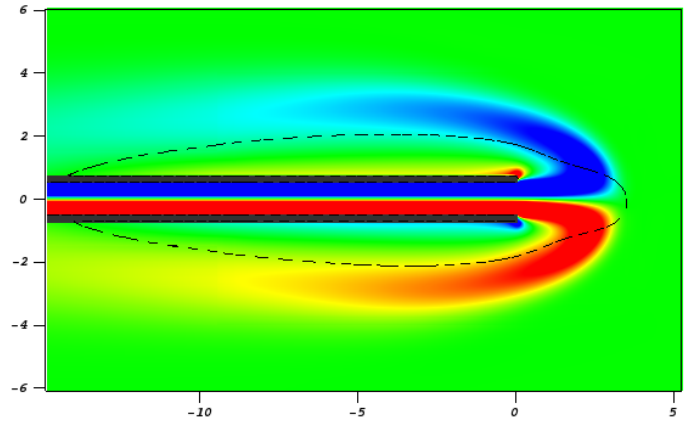

(c) $\alpha = 2.0$

Figure 4.4. The base flow states at different jet to counterflow velocity ratios. The vorticity contours are shown here. The dotted black surface represents the region where x-velocity = 0.

Stability of the jet is analyzed by computing the eigenvalues using the obtained base flow states. The search for global modes is performed using the block Krylov-Schur method. 2 blocks, each with a size of 30 resulting in a subspace dimension of 62 is used. The integration time between the snapshots is set to be equal to 1.2. The subspace method is interated till the residual reaches $< 10^{-4}$.

Numerical convergence is assessed by comparing the growth rate and frequency of the computed dominant eigenvalue. Table (4.1) shows the grid convergence for the case of $Re = 50$ jet at $\alpha = 1.7$. At three levels of refinement, the error in the computed growth rate is less than 2% and the error in frequency is less than 1%. All the simulations are performed on three levels of refinement. The simulations are run on 64 cores at the lonestar 5 and stampede supercomputers at Texas advances computing center (TACC). The simulations take around 6 hours including the base flow and the eigenvalue computations.

The computed spectrum of eigenvalues for different values of α is shown in figure (4.5). The spectrum shows that the low frequency modes are dominant. The shear modes are typically associated with high frequency. The centrifugal modes that are at the low frequency end of the spectrum are found to be dominant. The instability arises from the streamline curvature and we expect the loss of stability of

Levels of refinement	λ_r	λ_i	Error in λ_r	Error in λ_i
0	0.034	0.1743	–	–
1	0.0427	0.1692	20.3%	6.56%
2	0.04497	0.1664	5.1%	1.68%
3	0.0456	0.1655	1.38%	0.5%

Table 4.1. Convergence of eigenvalues for the case of $Re = 50$ and $\alpha = 1.7$. λ_r represents real part of eigenvalue (growth rate) and λ_i is imaginary part (frequency)

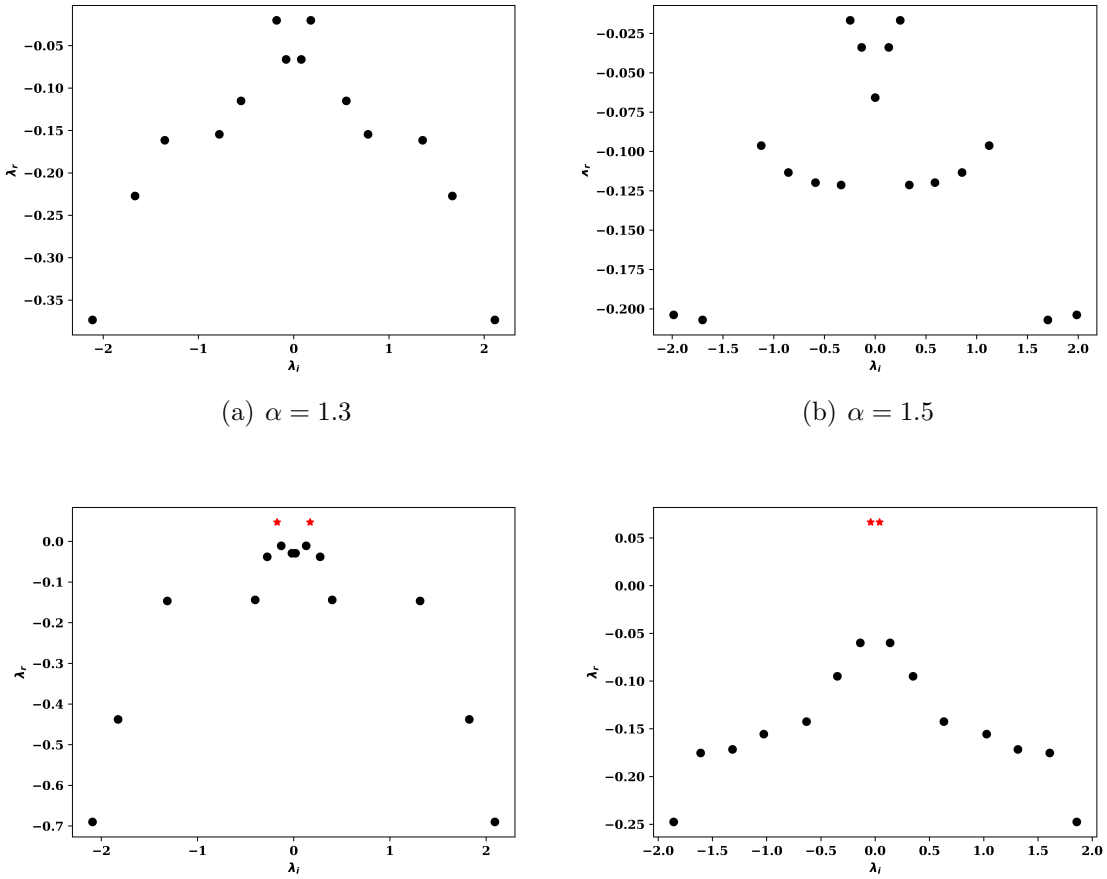

(a) $\alpha = 1.3$

(b) $\alpha = 1.5$

(c) $\alpha = 1.7$

(d) $\alpha = 2.0$

Figure 4.5. Spectrum of eigenvalues. X-axis shows the imaginary part and Y-axis shows the real part. Eigenvalues corresponding to the stable modes are shown in black while the ones corresponding to unstable modes are shown in red.

the two-dimensional base flow to three-dimensional instabilities as found by Barkley et al. [77] and by Brès and Colonius [78] in the case of recirculating flows. Tri-Global stability analysis of a planar jet in counterflow is being performed as the time of writing this thesis and the results will be published elsewhere. We also expect the growth rates associated with the shear modes to increase with Reynolds number leading to competetion between shear layer and centrifugal instability mechanisms. Stability analysis at such high Reynolds numbers is not performed in this thesis.

There is also the possibility of unstable wake modes leading to vortex shedding as seen in bluff body flows. However, the structural sensitivity analysis shows that the centrifugal instability is the dominant mechanism.

In an attempt to find the critical velocity ratio, the dominant eigenvalues are computed at different values of α. Figure (4.6) shows the variation of growth rate and frequency of the dominant eigenvalues at different velocity ratios. The growth rate of the leading eigenmode increases with the velocity ratio while its frequency decreases. The critical velocity ratio for the $Re = 50$ jet in counterflow at velocity ratio is found to be ≈ 1.60. Variation of the Strouhal number ($St \equiv \lambda_i \; D/2\pi U_{jet}$) with α is shown in figure (4.2). The dominant eigenmodes are shown in figures (4.7) and (4.8).

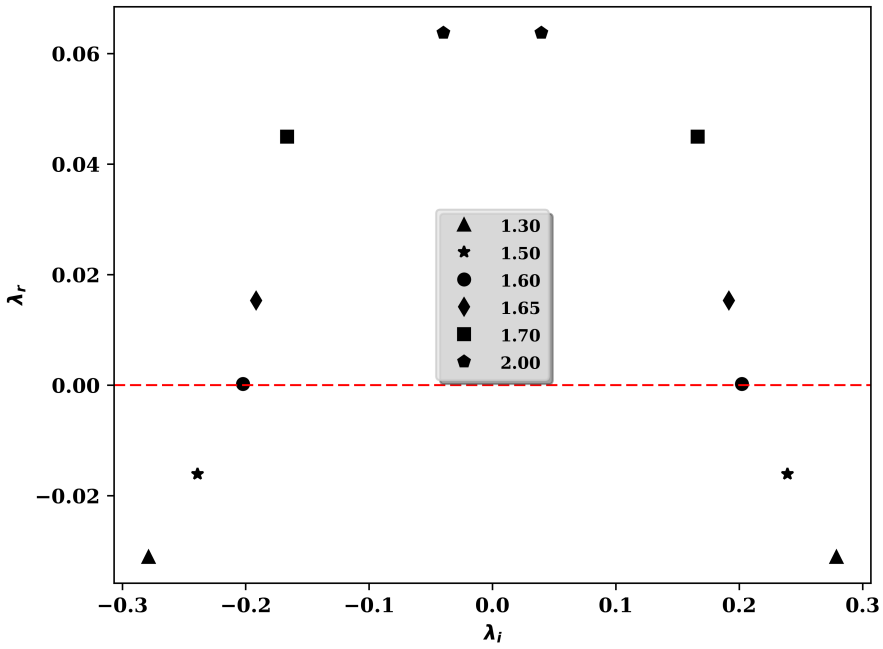

Figure 4.6. Dominant eigenvalues at different velocity ratios. X-axis shows the imaginary part and Y-axis shows the real part.

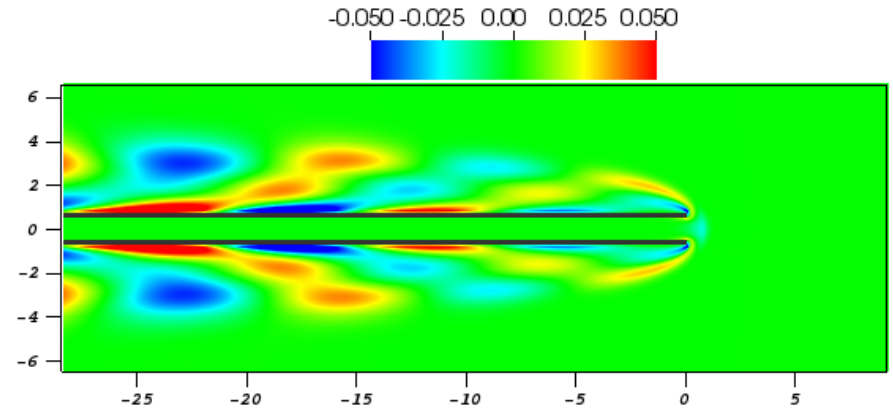

(a) $\alpha = 1.3$ (stable mode)

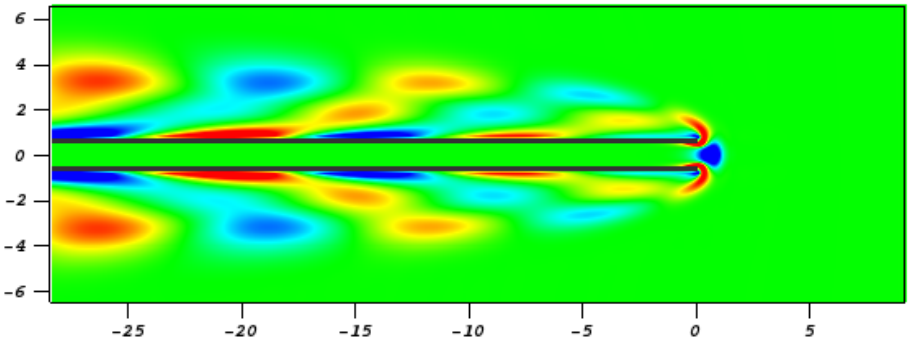

(b) $\alpha = 1.5$ (stable mode)

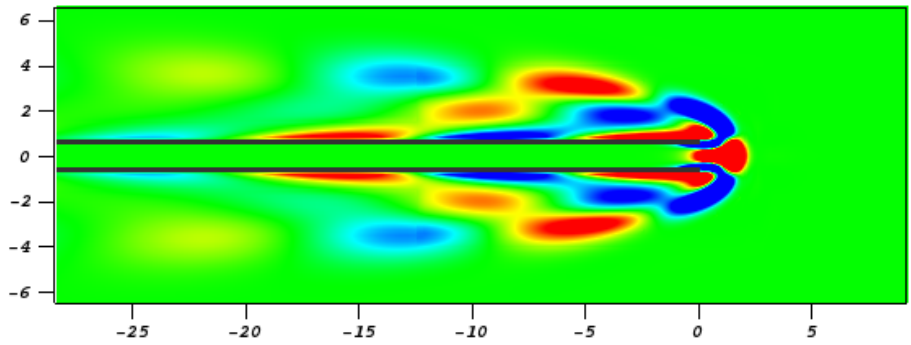

(c) $\alpha = 1.7$ (unstable mode)

Figure 4.7. Vorticity contour corresponding to the real part of the dominant direct mode computed at different values of α for $Re = 50$ jet.

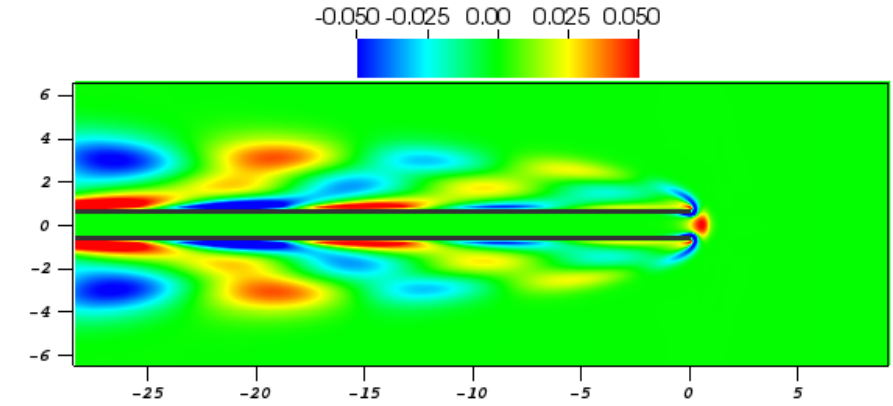

(a) $\alpha = 1.3$ (stable mode)

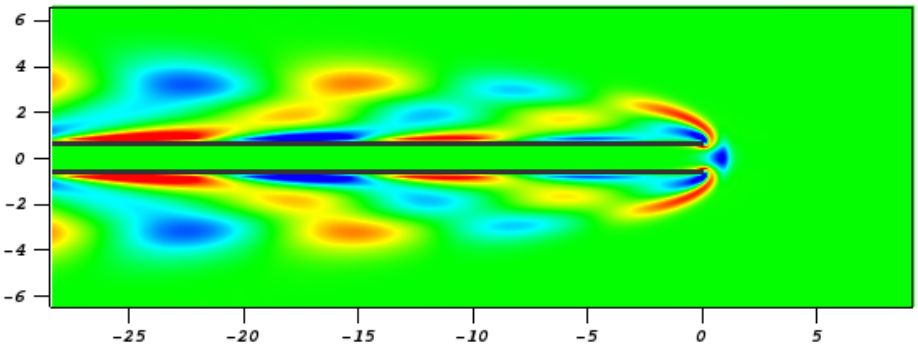

(b) $\alpha = 1.5$ (stable mode)

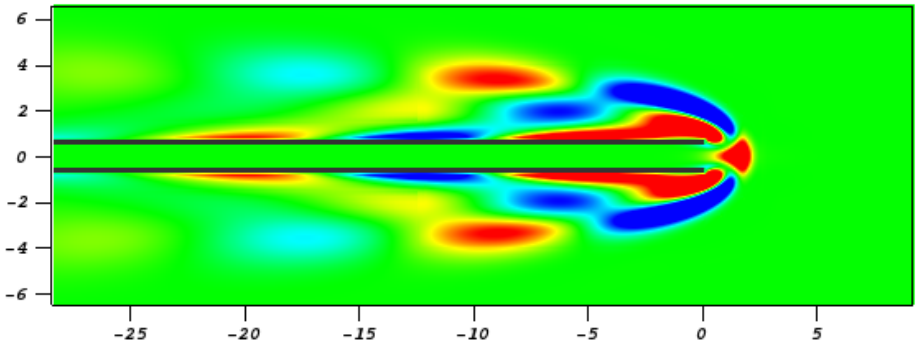

(c) $\alpha = 1.7$ (unstable mode)

Figure 4.8. Vorticity contour corresponding to the imaginary part of the dominant direct mode computed at different values of α for $Re = 50$ jet.

α	St
1.3	0.04439
1.5	0.03807
1.6	0.03051
1.7	0.026503
2.0	0.006316

Table 4.2. Variation of St with α

4.1.3 Stability of the jet at $Re = 75$

In this section, the stability analysis of the jet at $Re = 75$ is presented. Base flow state and the eigenvalues are obtained using the same procedure described in the previous section. The Reynolds number is changed by changing the viscosity and the effects of velocity ratio are analyzed. Figure (4.9) shows the computed base flow.

Figure (4.10) shows the specturm of eigenvalues and the variation of the growth rate and frequency of the most dominant eigenmode with velocity ratio is shown in

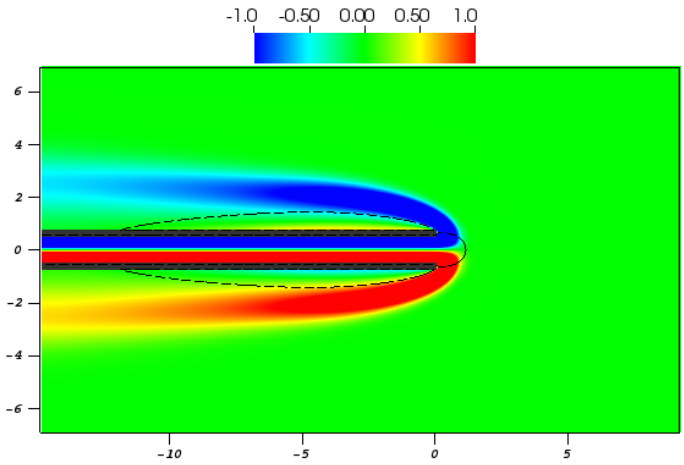

(a) $\alpha = 1.1$

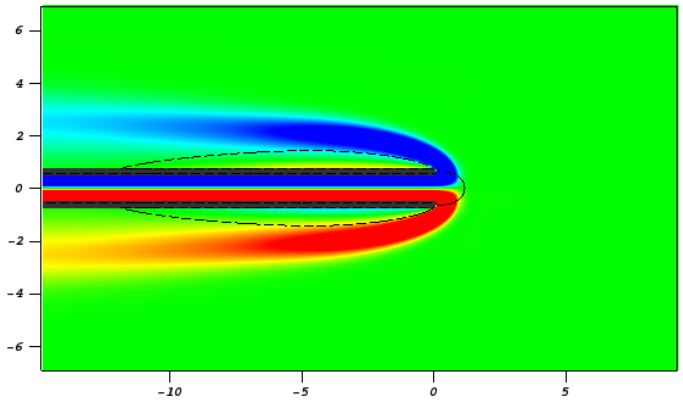

(b) $\alpha = 1.5$

Figure 4.9. The base flow states for $Re = 75$ at different jet to counterflow velocity ratios. The vorticity contours are shown here. The dotted black surface represents the region where x-velocity = 0.

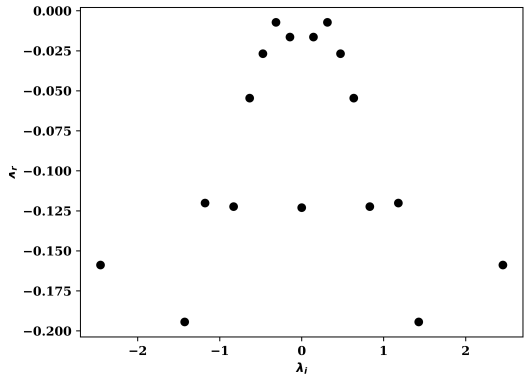

(a) $\alpha = 1.1$

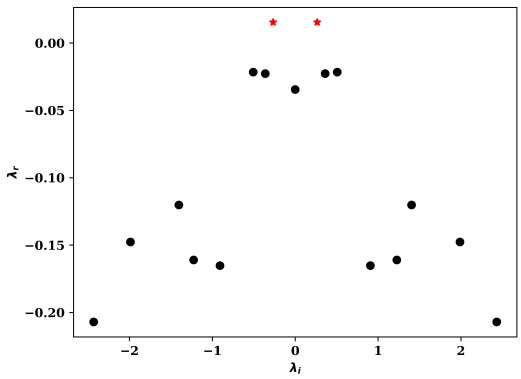

(b) $\alpha = 1.3$

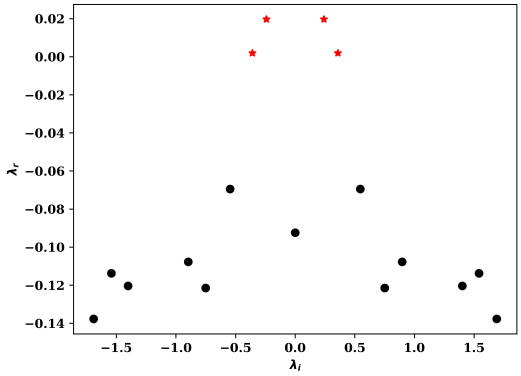

(c) $\alpha = 1.5$

Figure 4.10. Spectrum of eigenvalues for $Re = 75$. X-axis shows the imaginary part and Y-axis shows the real part. Eigenvalues corresponding to the stable modes are shown in black while the ones corresponding to unstable modes are shown in red.

figure(4.11). It can be seen that the jet becomes unstable at a velocity ratio between $1.1 - 1.3$, although the exact value is not determined. Multiple unstable modes are found at $\alpha = 1.5$. The Strouhal number reduces with velocity ratio and the variation is given in table (4.3). The St is similar to the values obtained for $Re = 50$ jet. The dominant eigenmodes are visualized in figures (4.12) and (4.13).

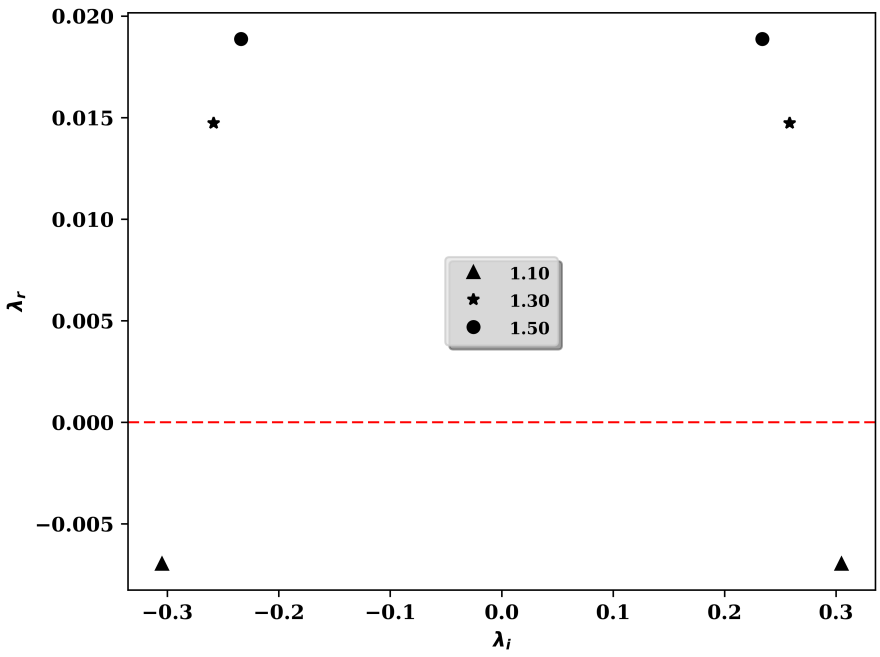

Figure 4.11. Dominant eigenvalues at different velocity ratios for $Re = 75$. X-axis shows the imaginary part and Y-axis shows the real part.

α	St
1.1	0.0485
1.3	0.0411
1.5	0.0372

Table 4.3. Variation of St with α for $Re = 75$

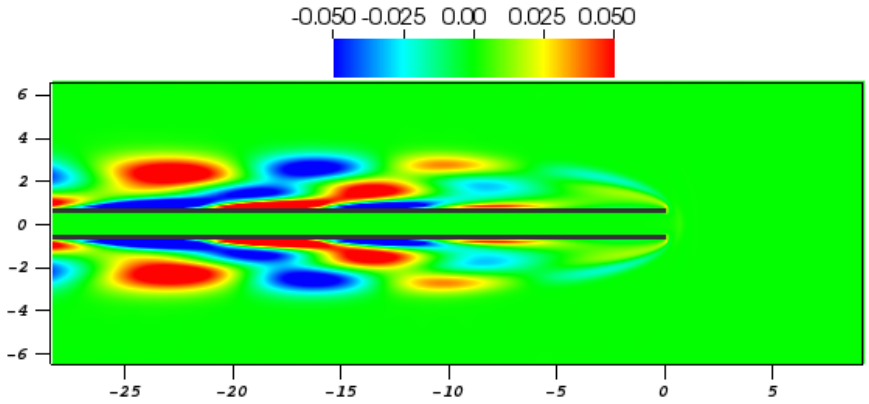

(a) $\alpha = 1.1$ (stable mode)

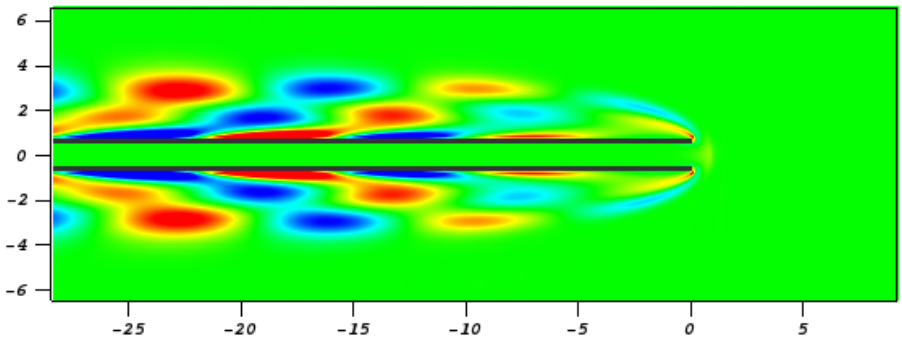

(b) $\alpha = 1.3$ (unstable mode)

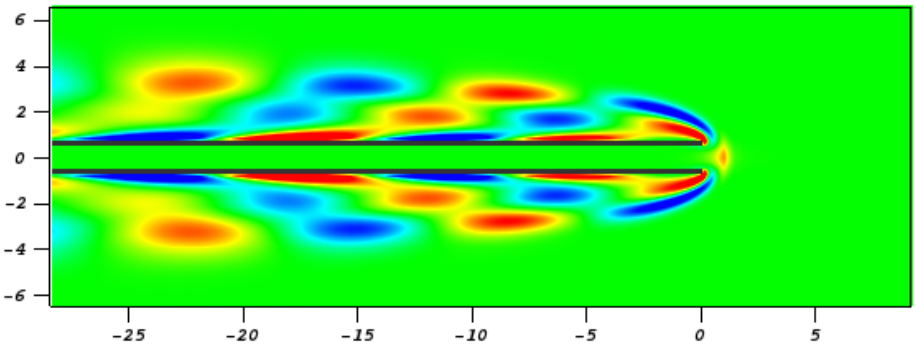

(c) $\alpha = 1.5$ (unstable mode)

Figure 4.12. Vorticity contour corresponding to the real part of the dominant direct mode computed at different values of α for $Re = 75$ jet.

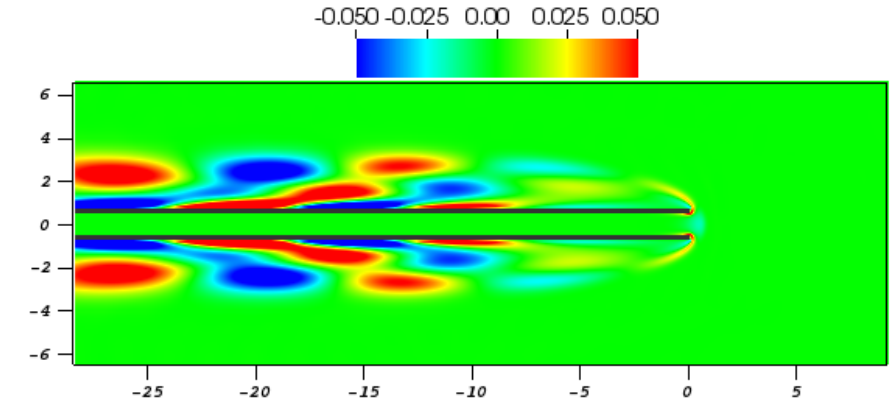

(a) $\alpha = 1.1$ (stable mode)

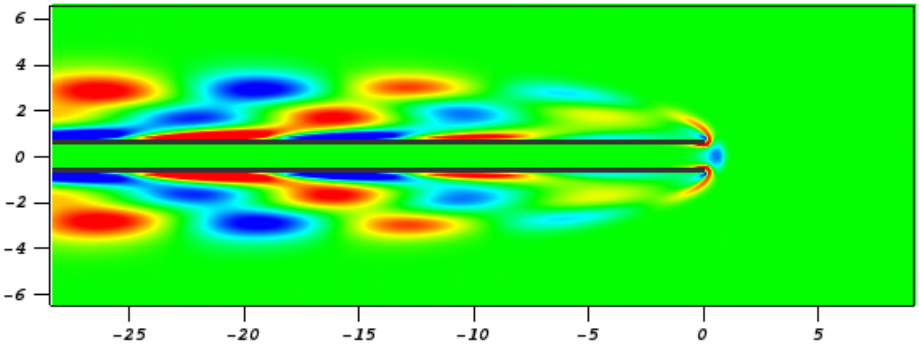

(b) $\alpha = 1.3$ (unstable mode)

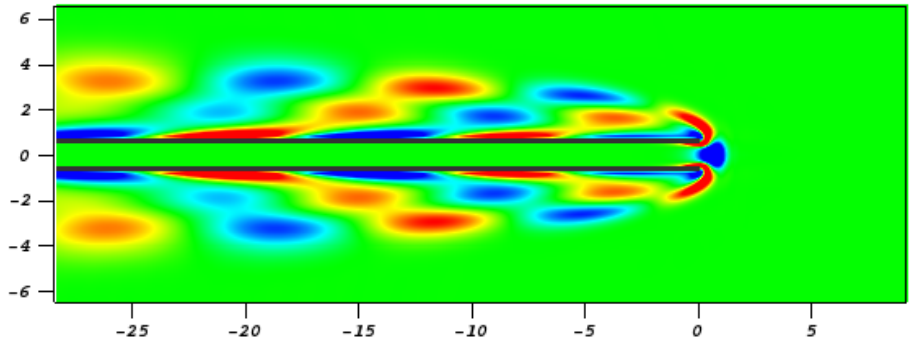

(c) $\alpha = 1.5$ (unstable mode)

Figure 4.13. Vorticity contour corresponding to the imaginary part of the dominant direct mode computed at different values of α for $Re = 75$ jet.

4.1.4 Stability of the jet at $Re = 100$

The stability of a jet at $Re = 100$ in counterflow is studied at a velocity ratio of 1.1 using the procedure described in previous sections. Figure (4.14) shows the computed base flow state and the spectrum of eigenvalues is shown in fig. (4.15).

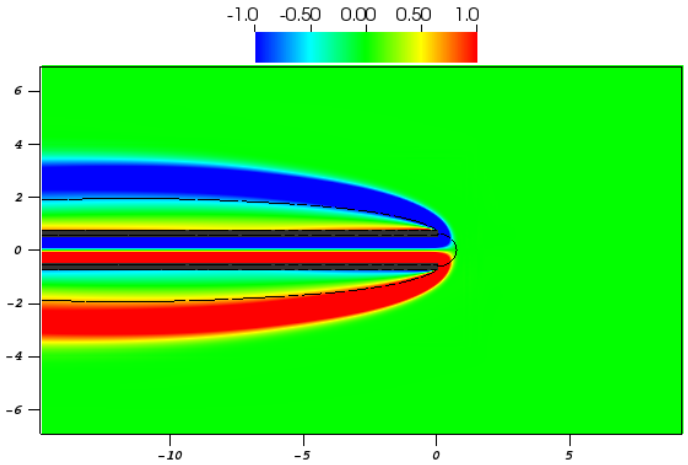

Figure 4.14. The vorticity contour of the base flow obtained for $Re = 100$ at $\alpha = 1.1$. The dotted black surface represents the region where x-velocity = 0.

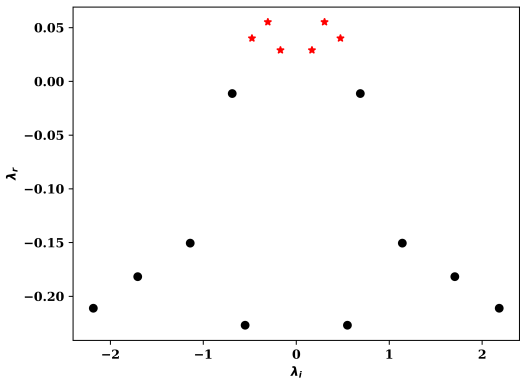

Figure 4.15. Eigen-specturm obtained for $Re = 100$ at $\alpha = 1.1$. X-axis shows the imaginary part and Y-axis shows the real part. Eigenvalues corresponding to the stable modes are shown in black while the ones corresponding to unstable modes are shown in red.

Multiple modes are unstable as seen in figure (4.15). The Strouhal number corresponding to the most dominant eigenmode is found to be 0.04712 which is very close to the value obtained for the jet at $Re = 75$. The dominant eigenmodes are shown in figure (4.16).

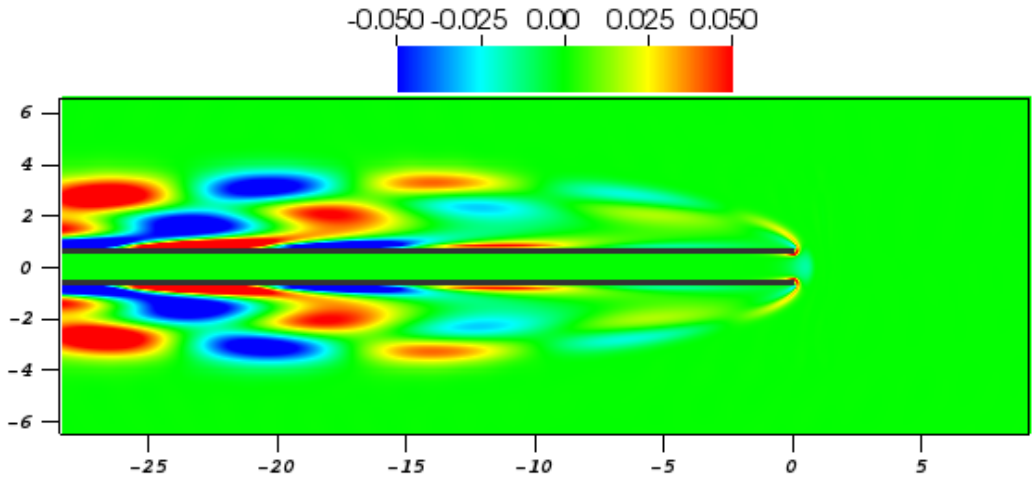

(a) Real part

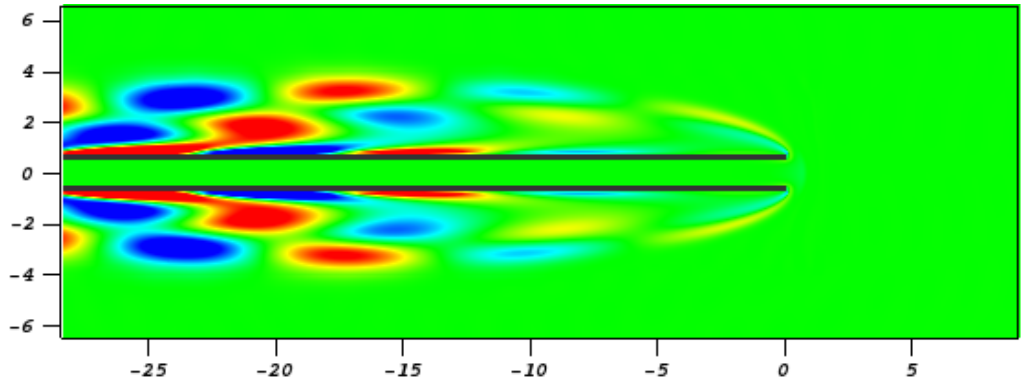

(b) Imaginary part

Figure 4.16. Vorticity contour of the dominant eigenmode obtained for $Re = 100$ at $\alpha = 1.1$.

4.1.5 Stability at velocity ratio = 1.5

Stability of the jet is analyzed at different Reynolds numbers, holding the velocity ratio constant at 1.5. The variation of the growth rate and frequency of the jet with Reynolds number is obtained and is shown in figure (4.17). It can be seen that the Reynolds number does not effect the frequency of the dominant mode. Bifurcation to unsteady state occurs at $Re \approx 62.5$.

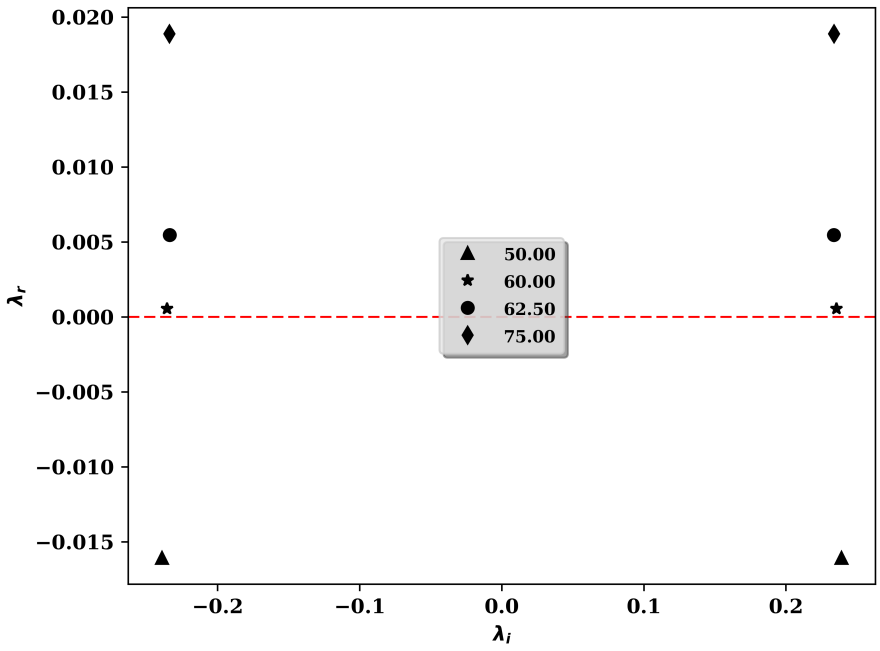

Figure 4.17. Dominant eigenvalues at different Reynolds numbers. X-axis shows the imaginary part and Y-axis shows the real part.

4.2 Tri-Global stability analysis of a round jet in counterflow

4.2.1 Problem setup

The schematic representation of the computational domain used to study the three-dimensional stability of a round jet in counterflow is provided in figure (4.18). The analysis is performed on the domain $[-32, -32, -32]$ x $[32, 32, 32]$. The jet enters the domain through a circular pipe of diameter, $D = 1$ unit and length, $L = 32$ units. The jet inlet is placed at the center of the $x = -32$ boundary. The thickness of the pipe considered is $0.25D$. The counterflow inlet in placed on the $x = 32$ boundary.

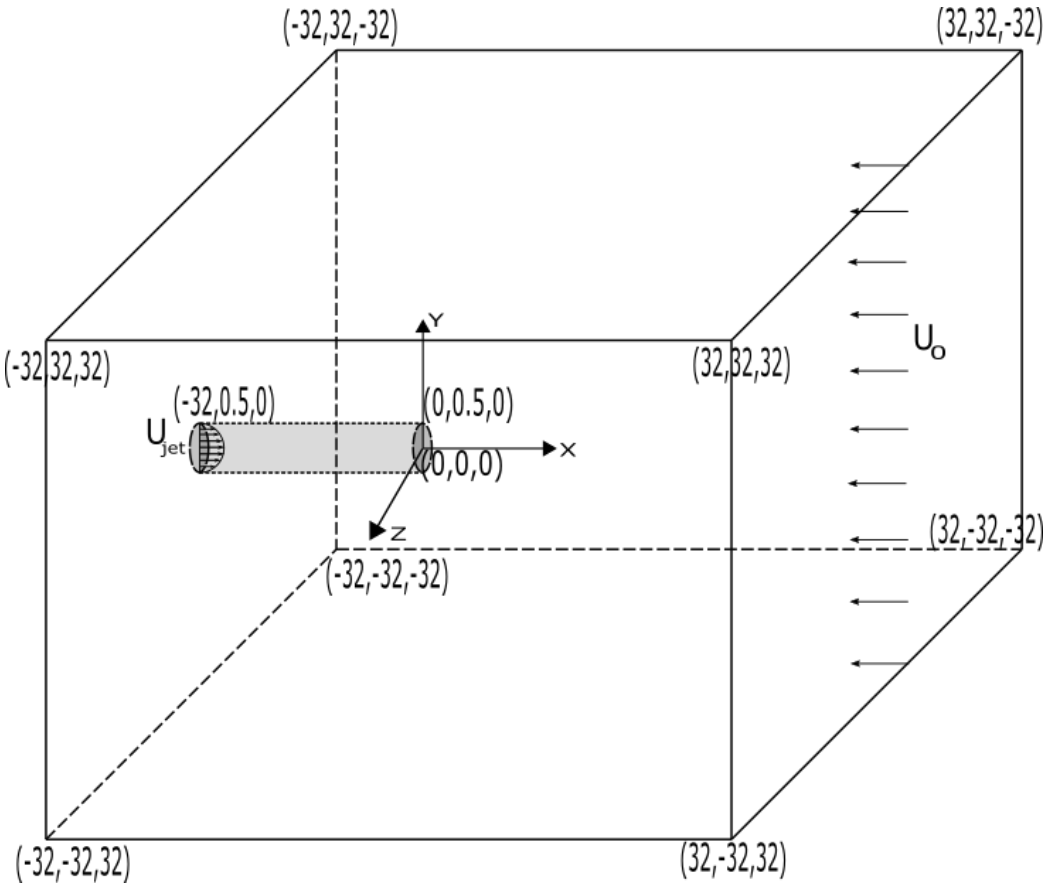

Figure 4.18. Schematic description of the computational setup used for stability analysis of round jet in counterflow.

At the jet inlet, a fully-developed parabolic profile with centerline velocity of $(2, 0, 0)$ is enforced during the base flow computation. At the counterflow inlet, the velocity is set to $(-U_0, 0, 0)$ and U_0 is changed to maintain the specified velocity ratio, α. The boundaries at $y = -32$, $y = 32$, $z = -32$ and $z = 32$ are modeled as farfield boundaries, where the velocity is set to be equal to the counterflow velocity, $(-U_0, 0, 0)$. The region outside the jet inlet at the $x = -32$ boundary is modeled as outflow. The pipe walls are treated as no-slip boundaries. During the eigenvalue computation, the velocity of perturbations is se to $(0, 0, 0)$ on all the boundaries.

The domain is discretized with a base mesh of resolution 256 x 256 x 256. The pipe walls are embedded into the cartesian mesh as shown in figure (4.19). Two levels of finer mesh with a refinement ratio of 2 are added at the regions where base flow vorticity, ω is greater than $0.5U_0/D$. A buffer region of two cells in added around each tagged cell for all levels of refinement.

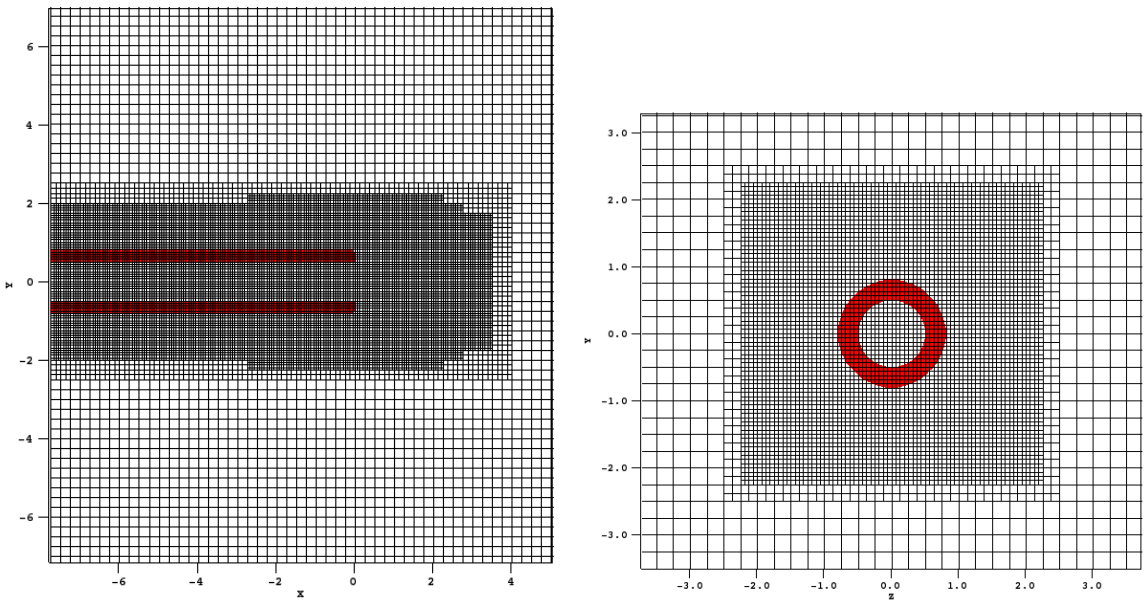

(a) Mesh on $Z = 0$ plane

(b) Mesh on $X = -2$ plane

Figure 4.19. Mesh used to discretize the computational domain. The embedded boundary representation of the pipe is shown in red.

4.2.2 Stability of round jet

Base flow is obtained using SFD technique. Adaptive scheme is not used and the parameters, (χ, Δ) are set to $(2, 1)$. Figure (4.20) shows the base flow computed for jet to counterflow velocity ratio of 3. The base flow is axisymmetric as expected.

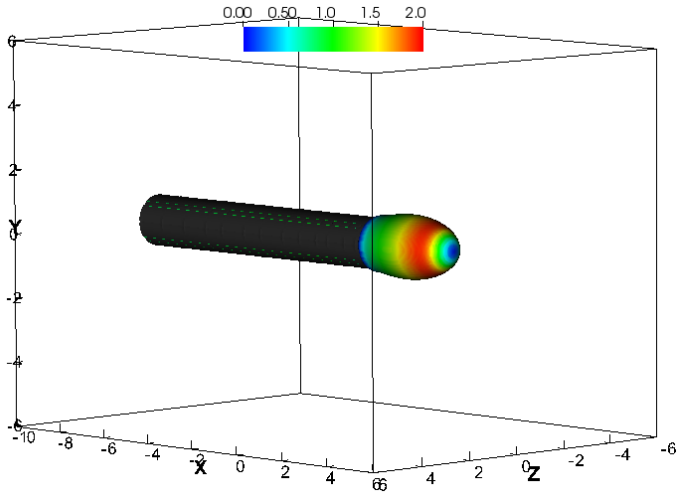

(a) Isosurface of x-velocity = 0, colored by vorticity magnitude

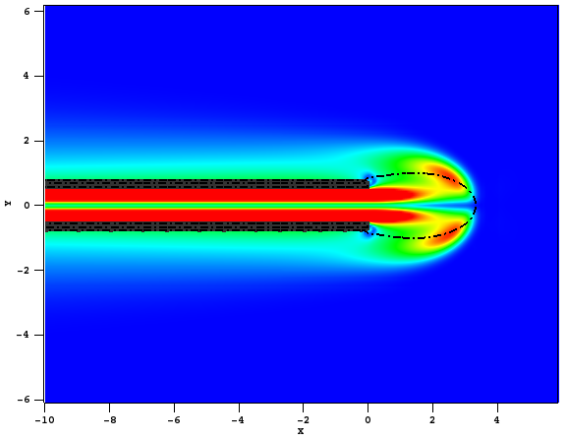

(b) Spanwise plane at $Z = 0$

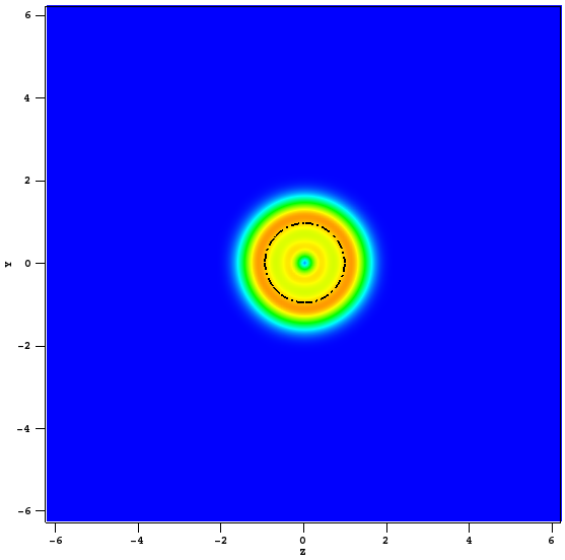

(c) Streamwise plane at $X = 2$

Figure 4.20. Contour of base flow vorticity obtained for $Re = 50$ round jet at velocity ratio of 3. Black surface in (b) and (c) represents contour of x-velocity = 0.

The axial penetration length is found to be ≈ 4 and the radial extent of penetration is ≈ 2. At higher velocity ratios and Reynolds numbers, the base flow could not be obtained using SFD and the Newtons method is computationally expensive due to slow convergence. In this thesis, only the analysis of $Re = 50$ round jet at $\alpha = 3.0$ is presented.

The obtained baseflow is used to compute the eigenvalues. The block Krylov-Schur method with 1 block of 63 vectors, resulting in a subspace dimension of 64 is used to obtain the eigenvalues. Integration time between the snapshots is set to 2.4. The method is iterated till the residual reaches $< 10^{-4}$. Numerical convergence is assessed by comparing the computed dominant eigenvalue on different levels of refinement as shown in table (4.4). The error in the growth rate between 3 and 2 levels is found to be 5.4%. The accuracy is comprimised to save computational time and the analysis is performed on the mesh with 2 levels of refinement. The simulations take around 20 hours on 1200 cores at the lonestar 5 supercomputer at TACC.

Figure (4.21) shows the computed eigen-spectrum. All the obtained modes are stable. The presence of two stationary modes in the spectrum can be observed. At higher Reynolds numbers and velocity ratios, we expect the stationary modes to be dominant with positive growth rates. This explains why SFD method failed to

Levels of refinement	λ_r	λ_i	Error in λ_r	Error in λ_i
0	-0.03581	0.3874	–	–
1	-0.02906	0.3576	23.2%	8.4%
2	-0.0259	0.3448	12.2%	3.7%
3	-0.02457	0.3378	5.4%	2.1%

Table 4.4. Convergence of eigenvalues for the case of $Re = 50$ round jet at $\alpha = 3.0$. λ_r represents real part of eigenvalue (growth rate) and λ_i is imaginary part (frequency)

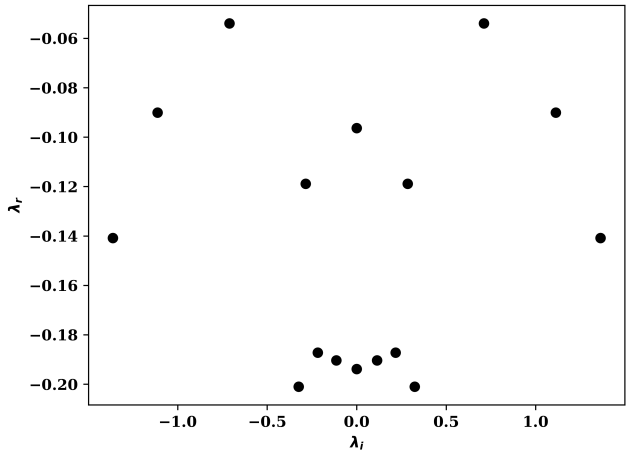

Figure 4.21. Spectrum of eigenvalues obtained for a round jet at $Re = 50$ and $\alpha = 3.0$. X-axis shows the imaginary part and Y-axis shows the real part.

converge to base flow. Unsteady simulation performed at $Re = 100$ showed shedding of vortex rings as shown in figure (4.22). Compared to the two-dimensional planar jet at $Re = 50$ which becomes unstable at $\alpha = 1.6$, a round jet is found to be stable even at $\alpha = 3.0$. This could be due to the different velocity profile in a round

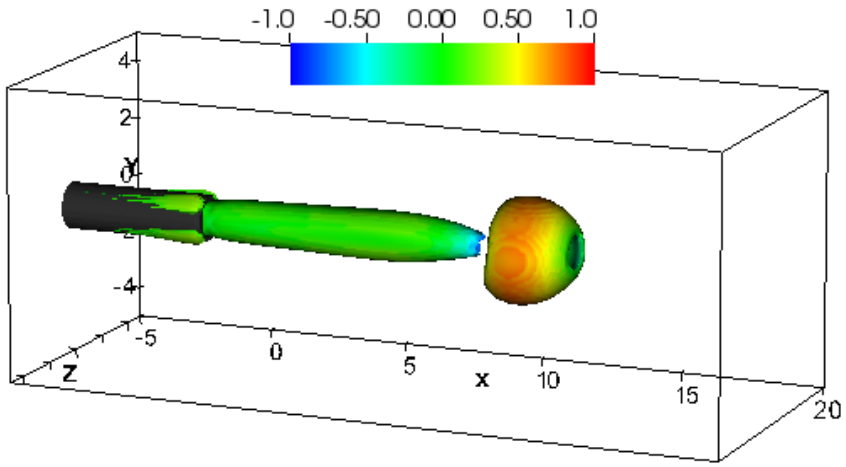

Figure 4.22. Snapshot from unsteady run for the case of a round jet at $Re = 100$ and $\alpha = 3.0$. Isosurface of vorticity magnitude = 1, colored by x-velocity is shown here.

pipe when compared to planar channel. The Strouhal number corresponding to the most dominant mode is found to be 0.055 which is slightly higher than that of two-dimensional planar jet. The dominant eigenmodes are visualized in figure (4.23).

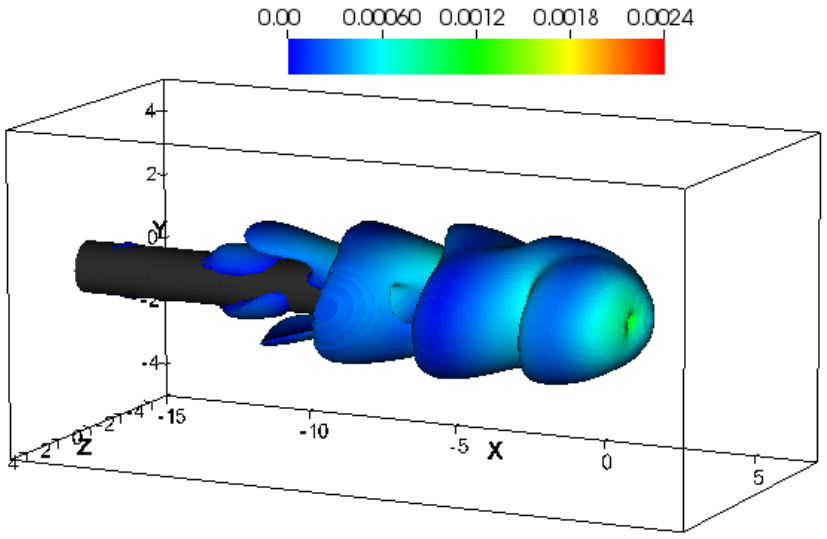

(a) Real part

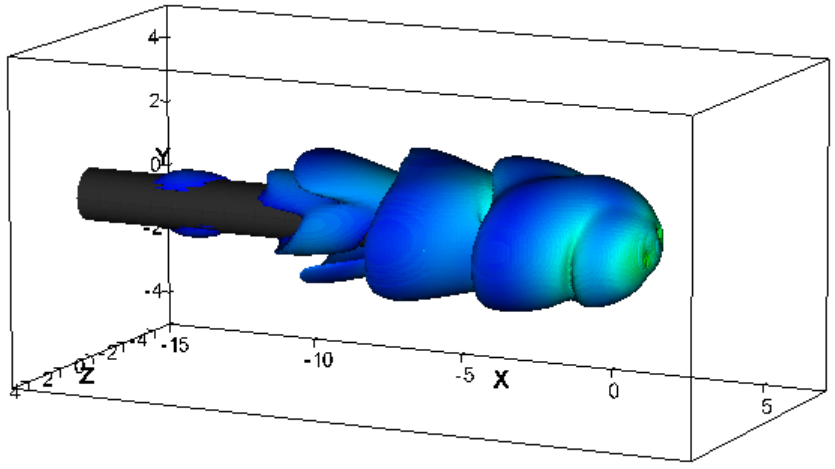

(b) Imaginary part

Figure 4.23. Isosurface of vorticity = 0.001 corresponding to the dominant eigenmode obtained for $Re = 50$ round jet at $\alpha = 3.0$. The isosurface is colored by the perturbation velocity magnitude.

4.3 Chapter summary

The asymptotic stability analysis of jet in counterflow is presented in this chapter. The effect of Reynolds number and jet to counterflow velocity ratio on the stability of a two-dimensional planar jet is investigated. The low frequency modes are observed to be dominant. The Strouhal number correspnding to the most dominant modes is found to be around $0.04 - 0.006$ for the range of Reynolds numbers and velocity ratios considered. The instability arises from the streamline curvature similar to the centrifugal instability mechanism found in the case of recirculating flows. Approximate critical velocity ratio values for a two-dimenisonal planar jet are obtained as shown in table (4.5).

Re	$\alpha_{critical}$
50	1.6
62.5	1.5
75	1.1 – 1.3
100	< 1.1

Table 4.5. Critical velocity ratio at different jet Reynolds number

The stability analysis of a round jet at $Re = 50$ showed that the jet is stable at velocity ratio of 3. The presence of standing modes in the computed spectrum is observed. At higher Reynolds numbers, the standing modes become dominant and shedding of axisymmetric vortex rings is observed.

CHAPTER 5

TRANSIENT GROWTH ANALYSIS

In the previous chapter, the aymptotic stability of a jet in counterflow is analyzed by computing the eigenvalues. However, the eigenvalue analysis is not sufficient to describe the stability when the non-normal effects are important. In this chapter, the transient growth of perturbations is analyzed by computing the eigenvalues of the symmetric operator resulting from the product of linear Navier-Stokes operator and its adjoint, as described in chapter 2. The optimal initial perturbations that lead to maximum transient growth are obtained.

5.1 Analysis of two-dimensional planar jet in counterflow

This section presents the transient growth of perturbations in the case for a two-dimenisonal planar jet in counterflow. The computational domain used for the analysis is described in section (4.1.1). As described in chapter 2, transient growth analysis requires solution to the linear perturbation equations and the adjoint equations. The Neumann outflow boundary condition enforced on forward evolution of perturbations requires implementation of Robin boundary conditions on the adjoint perturbations. In this thesis, homogeneous Dirichlet boundary conditions on perturbation velocity is enforced at all boundaries. It is assumed that the outflow boundary is sufficiently far away so that the boundary conditions do not effect the evolution of perturbations.

The transient growth of perturbations and the optimal initial perturbations are evaluated at different time horizons, τ. The eigenvalues are obtained using the

block Krylov-Schur method. The snapshots that span the subspace are obtained by integrating the linear perturbation solver by τ and using this solution as initial condition to integrate the adjoint solver by τ. The subspace dimension is set to 12 and the most dominant eigenmode is obtained within 12 iterations. The transient growth of perturbations for the case of $Re = 50$ and $Re = 75$ jet is presented in the following sections.

5.1.1 Analysis of jet at $Re = 50$

In this section, the transient growth is analyzed at different velocity ratios by fixing the jet Reynolds number at 50. The base flow states are obtained using the adaptive SFD method as described in the section (4.1.2). The transient energy growth of perturbations at different time horizons is shown in figure (5.1). The optimal mode

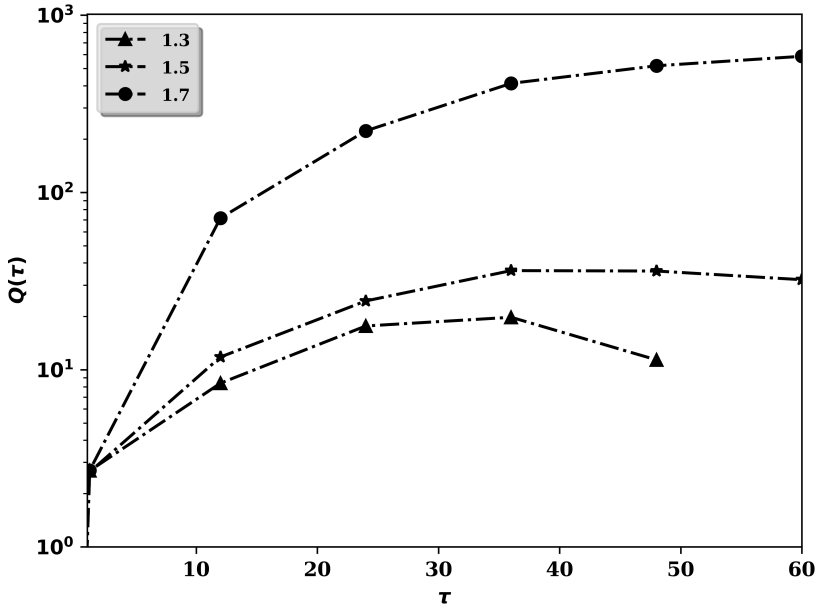

Figure 5.1. Transient energy growth of perturbations for $Re = 50$ two-dimensional planar jet.

at $\alpha = 1.3$ amplifies by a factor of ≈ 25 at $\tau \approx 30$ after which the energy mode starts decaying. The maximum amplification at $\alpha = 1.5$ occurs at $\tau \approx 40$. In this time horizon, the optimal mode amplifies by a factor of ≈ 37. At $\alpha = 1.7$, the energy amplification is rapid during the short time horizon and it asymptotically reaches the rate determined by the eigenvalue.

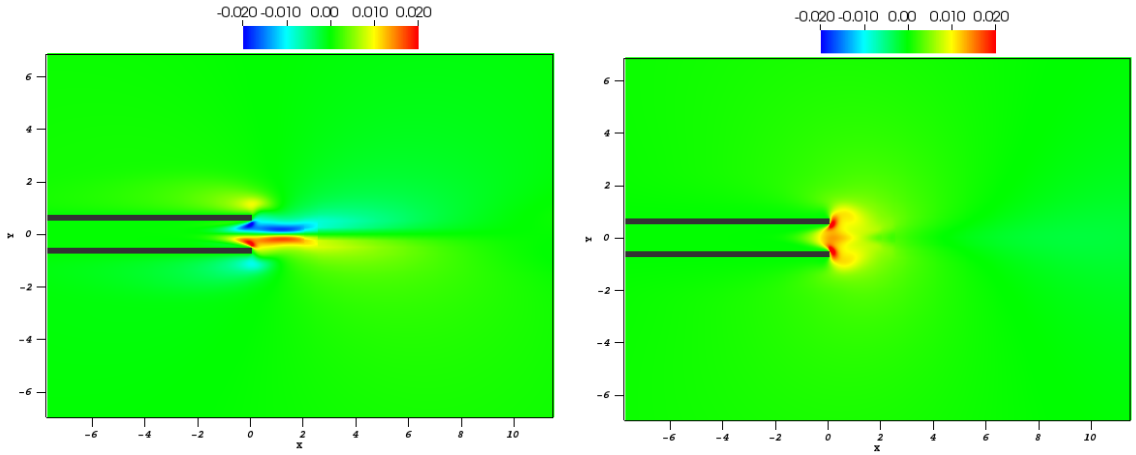

(a) x-velocity (b) y-velocity

Figure 5.2. Velocity contour of the optimal initial perturbation that leads to maximum energy growth at $\tau = 24$ for the case of planar jet at $Re = 50$ and $\alpha = 1.7$.

The optimal initial perturbation at $\alpha = 1.7$ for $\tau = 24$ is shown in figure (5.2). The optimal mode is located at the jet exit and its spatial position does not appear to change with τ. This shows that the transient growth mechanism is related to the compression of the jet column. There is also a convective subdominant mode with energy amplification at $\alpha = 1.7$. The energy of the identified subdominant mode amplifies by a factor of ≈ 58 at $\tau = 24$. However, this mode is expected to decay at a longer time horizon as the eigenvalue analysis predicts only one unstable mode at $\alpha = 1.7$. The subdominant mode is shown in figure (5.3).

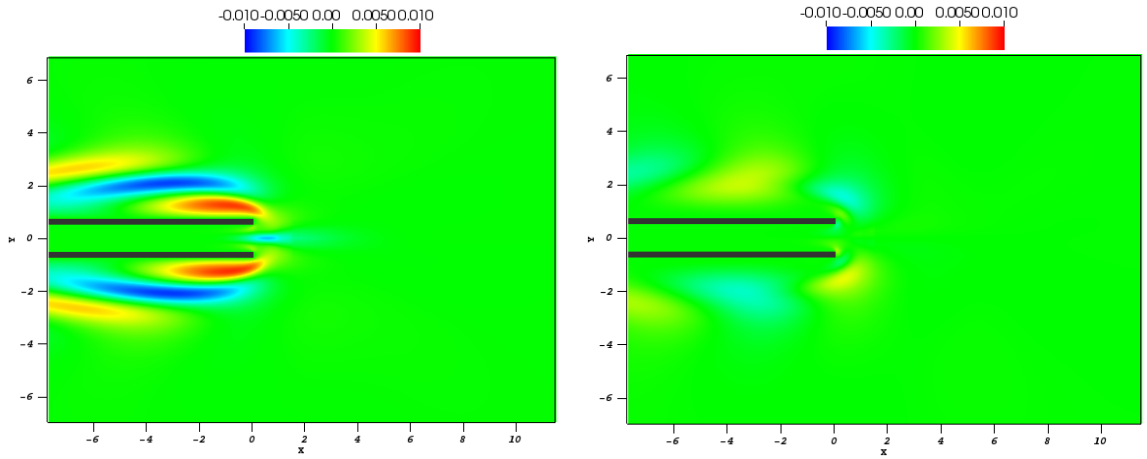

(a) x-velocity (b) y-velocity

(c) x-velocity (d) y-velocity

Figure 5.3. Velocity contour of the subdominant convective mode with energy amplification for the case of planar jet at $Re = 50$ and $\alpha = 1.7$. (a), (b) correspond to $\tau = 12$ and (c), (d) correspond to $\tau = 24$.

5.1.2 Analysis of jet at $Re = 75$

The transient growth of perturbations is analyzed for the case of planar two-dimensional jet at $Re = 75$ in this section. The base flow used for the analysis is shown in figure (4.9). The energy amplification over $\tau = 24$ is analyzed at velocity ratios of 1.1 and 1.3. Figure (5.4) shows the energy amplification at different time horizons. The energy amplification at $\alpha = 1.3$ is more than the amplification at $\alpha = 1.3$. The optimal initial mode at $\alpha = 1.1$ amplifies by a factor of 560 while the optimal mode amplifies by 410 at $\alpha = 1.3$ over a time horizon of 24. However, the amplification for the case of $\alpha = 1.1$ is expected to reach a maximum value before starting to decay at a longer time horizon, as all the eigenvalues for this configuration are found to be stable. The optimal modes at $\alpha = 1.3$ are shown in figure (5.5). The modes are located close to the jet exit and the spatial position does not appear

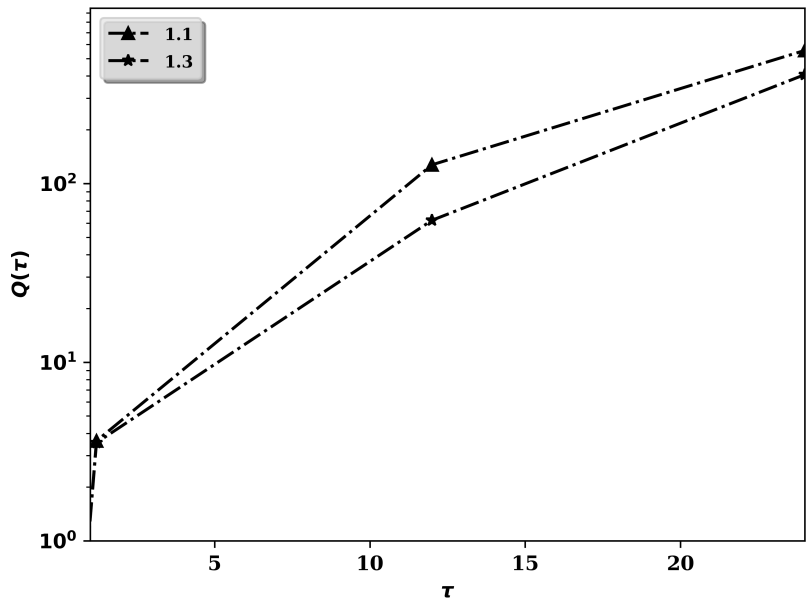

Figure 5.4. Transient energy growth of perturbations for $Re = 75$ two-dimensional planar jet.

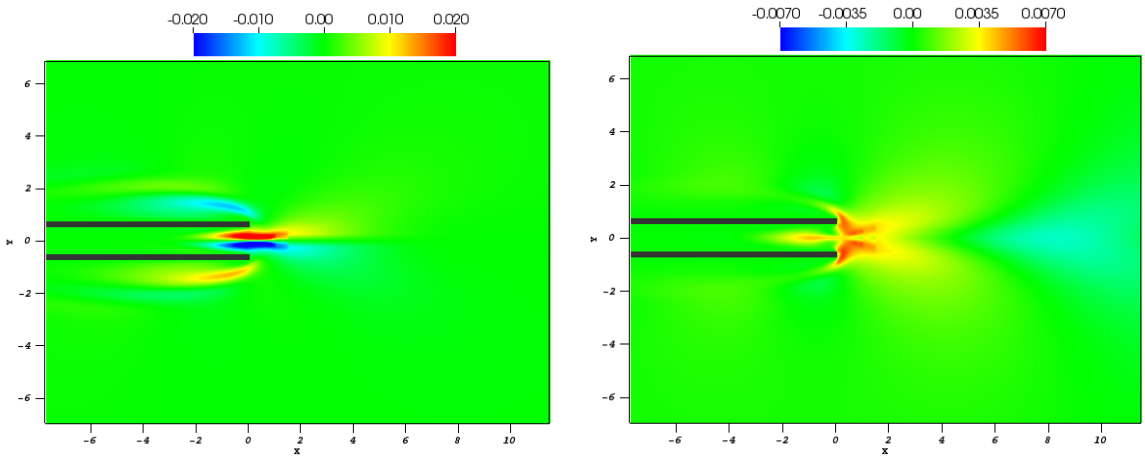

(a) x-velocity (b) y-velocity

Figure 5.5. Velocity contour of the optimal initial perturbation that leads to maximum energy growth at $\tau = 24$ for the case of planar jet at $Re = 75$ and $\alpha = 1.3$.

to change with τ as observed in the case of $Re = 50$ jet. These findings further suggest that the transient growth mechanism is related to the compression of the jet column. It is not clear from this analysis if the jet compression can support feedback mechanism and change the global behavior of the jet.

5.2 Analysis of round jet at $Re = 50$ and $\alpha = 3$

The transient growth of three dimensional perturbations is analyzed for the case of a round jet at $Re = 50$ and $\alpha = 3$. The computational domain used for the analysis is described in section (4.2.1). Homogeneous Dirichlet boundary conditions are enforced on perturbations at all boundaries of the domain. The analysis is performed on the mesh with two levels of refinement as shown in figure (4.19). Transient growth of perturbations is obtained using the Krylov-Schur method with a subspace dimension of 12 obtained by setting 1 block with 11 vectors.

The amplification of optimal initial perturbations at different time horizons is shown in figure (5.6). The maximum energy amplification factor is found to be around

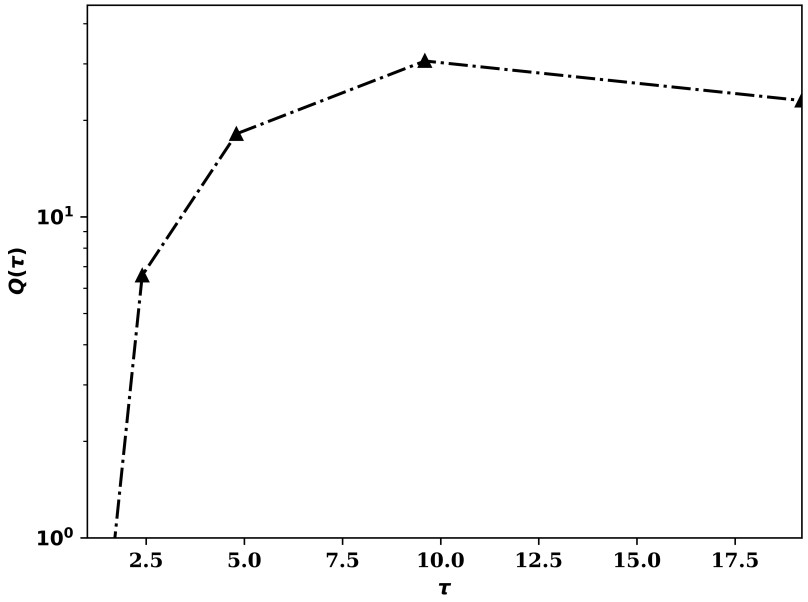

Figure 5.6. Transient energy growth of perturbations for the case of a round jet at $Re = 50$ and $\alpha = 3$.

35 at $\tau \approx 10$. At $\tau > 10$, the perturbation energy decays which is consistent with the finding that all the eigenvalues for this configuration are found to be stable. At higher Reynolds numbers, we expect the amplification to significantly increase. The effect of velocity ratio is not clear as the transient growth mechanism arising from the compressed jet column has complex dependence on both Re and α. Figure (5.7) presents the initial optimal perturbation in terms of the perturbation vorticity magnitude colored by the velocity magnitude. As the jet column gets compressed by the counterflow, there seems to be a rotation of the optimal perturbations about the x-axis.

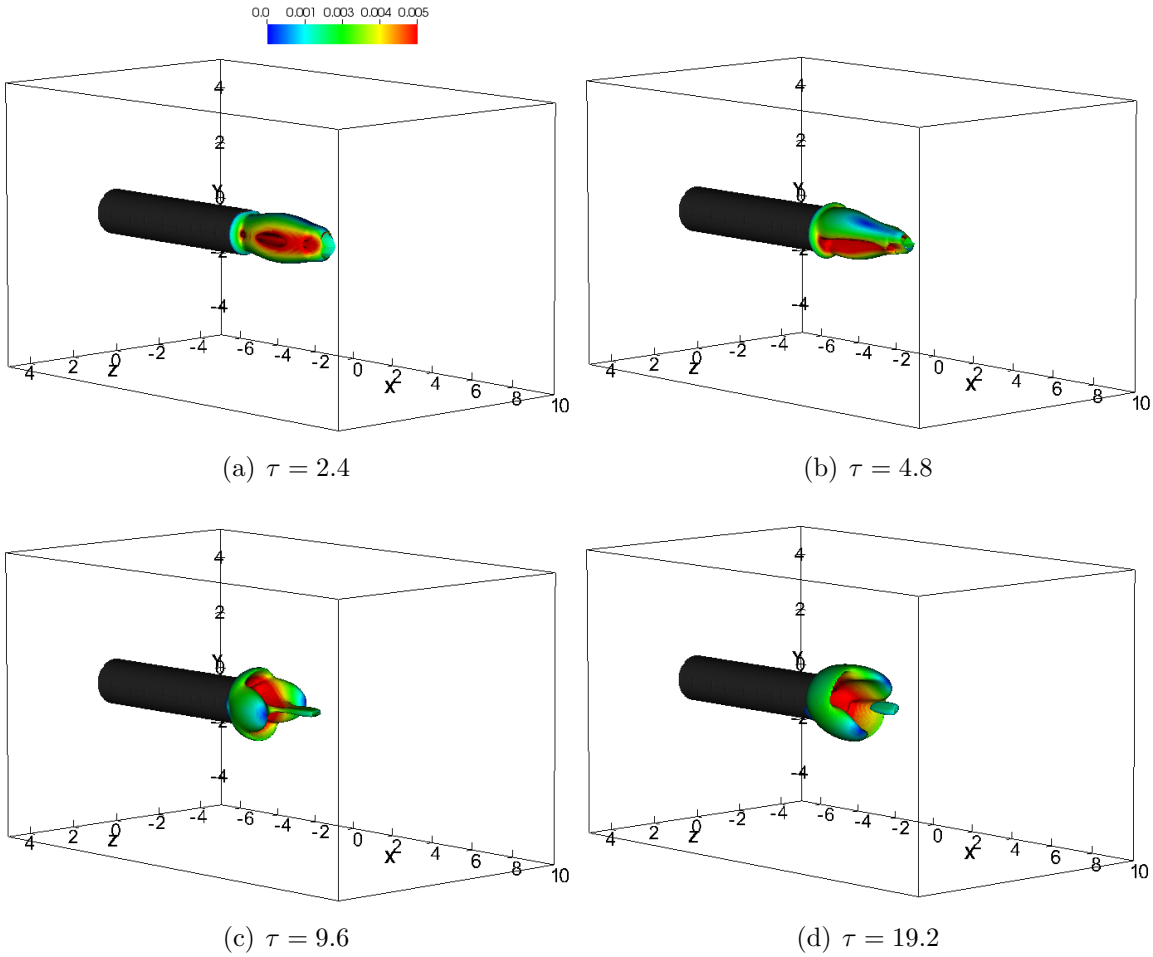

(a) $\tau = 2.4$ (b) $\tau = 4.8$

(c) $\tau = 9.6$ (d) $\tau = 19.2$

Figure 5.7. Initial optimal perturbation at different time horizons for a round jet at $Re = 50$ and $\alpha = 3$. Isosurface of vorticity $= 0.01$, colored by the velocity magnitude is shown here.

5.3 Chapter summary

The transient growth analysis of the flowfield of a jet in counterflow is presented in this chapter. The analysis has been applied to two-dimensional planar jet at $Re = 50$ and $Re = 75$ and round jet at $Re = 50$. The analysis shows the presence of non-normal effects of the Navier-Stokes operator, leading to transient energy amplification of perturbations even for the cases that are predicted to be stable by the eigenvalue analysis. The energy amplification factor for the case of planar jet at $Re = 50$ is found to be ≈ 40 at $\alpha = 1.5$. At $\alpha = 1.7$, the rapid initial energy amplification

asymptotically reaches the growth rate determined by the dominant eigenvalue. The presence of a subdominant mode with energy amplification is identified at $\alpha = 1.7$.

At $Re = 75$, the energy amplification factor is more than 500 at time horizon of 24 for $\alpha = 1.1$. It can be seen that the amplification for the case of $\alpha = 1.1$ in the investigated time horizon is greater than that of $\alpha = 1.3$. For the case of a round jet, the maximum energy amplification is found to be ≈ 30 at $\alpha = 3$.

The optimal initial perturbations are visualized. The optimal mode is located at a fixed spatial region in the investigated time horizons. It is hypothesized that the transient growth mechanism arises from the compression of the jet column.

CHAPTER 6

STRUCTURAL SENSITIVITY ANALYSIS

This chapter presents the structural sensitivity of a jet in counterflow. The sensitivity of two-dimensional flowfield associated with planar jet at $Re = 50$ and $Re = 100$ and the three-dimensional flowfield associated with round jet at $Re = 50$ is analyzed. The adjoint eigenmodes are computed. The wavemaker region is revealed by overlapping the adjoint eigenmodes with the direct eigenmodes. The region in the flowfield where the growth rate and the frequency of the leading eigenmode are most reciptive to structural modifications in the base flow is identified.

6.1 Structural sensitivity of two-dimensional planar jet in counterflow

This section presents the structural sensitivity of a two-dimensional planar jet in counterflow. The computational domain used for the analysis is described in section (4.1.1). Homogeneous Dirichlet boundary conditions are enforced on the adjoint perturbations at all boundaries of the domain. The analysis is preformed on three levels of refined mesh as shown in figure (4.3). The adjoint modes are computed using the same procedure used to obtain the direct modes as described in section (4.1.2). The span of the subspace is obtained from the adjoint equations solver.

The most dominant adjoint eigenmode obtained for the case of $Re = 50$ jet at $\alpha = 1.7$ is shown in figure (6.1). The corresponding eigenvalue is found to be $0.041 \pm 0.1572i$. The most dominant direct mode for this configuration is shown in figure (4.7(c)) and the corresponding eigenvalue is $0.042 \pm 0.161i$.

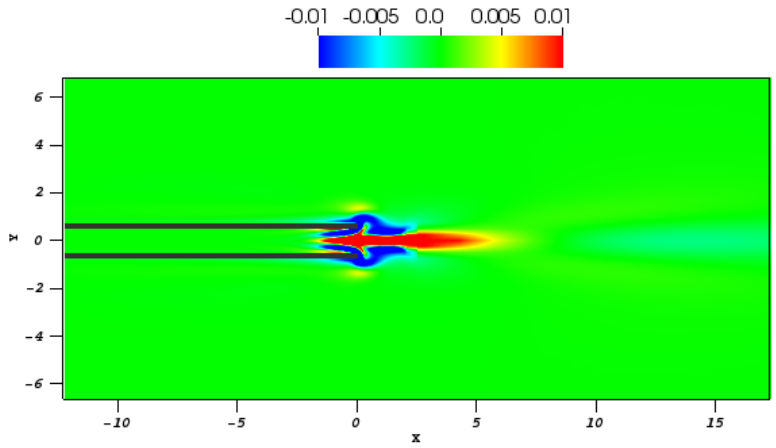

(a) Real part

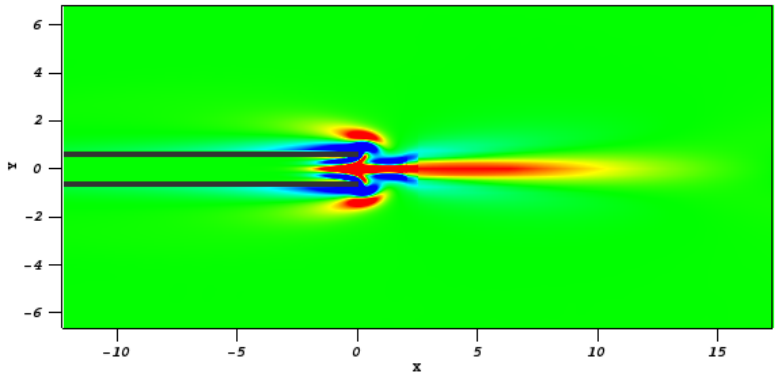

(b) Imaginary part

Figure 6.1. Vorticity contour of the adjoint mode obtained for the case of planar jet at $Re = 50$ and $\alpha = 1.7$.

The region in the flowfield where the growth rate of the leading eigenmode is most recip tive to modifications in the structure of the base flow is obtained from the overlap of the real part of direct and adjoint modes. Similarly, the region where the frequency is most receptive is found from the imaginary part of the direct and adjoint modes. The overlap region is obtained using the norm given by (2.22). This overlap region is known as wavemaker. The computed wavemaker region for $Re = 50$ planar jet at $\alpha = 1.7$ is shown in figure (6.2).

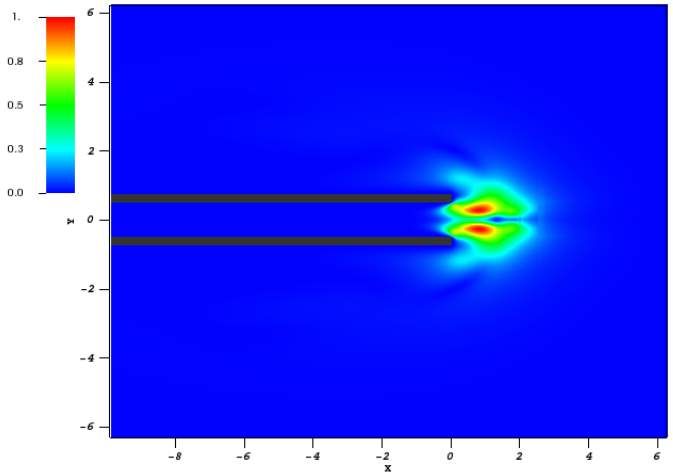

(a)

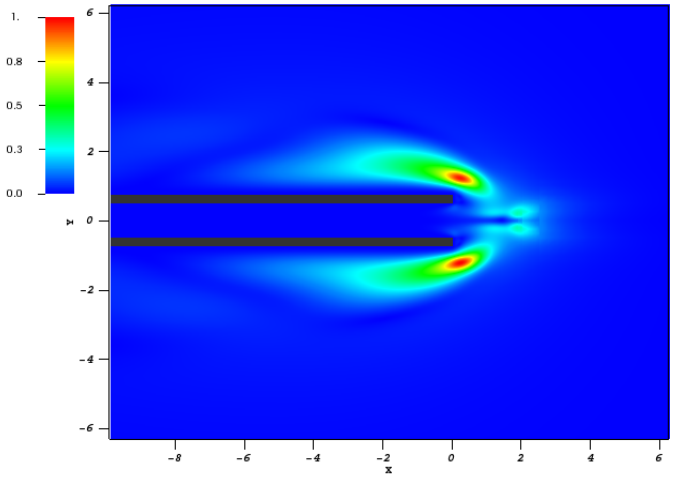

(b)

Figure 6.2. Wavemaker region obtained for planar jet at $Re = 50$ and $\alpha = 1.7$. (a) shows region where growth rate is most sensitive and (b) shows region where frequency is most sensitive.

Similar analysis is performed for the case of the planar jet at $Re = 100$ and $\alpha = 1.1$. The eigenvalue corresponding to the leading adjoint mode is found to be $0.0519 \pm 0.291i$. The leading adjoint mode is shown in figure (6.3). The most dominant direct mode for this configuration is shown in figure (4.16) and the corresponding

eigenvalue is $0.053 \pm 0.296i$. The computed wavemaker region for this configuration is shown in figure (6.4).

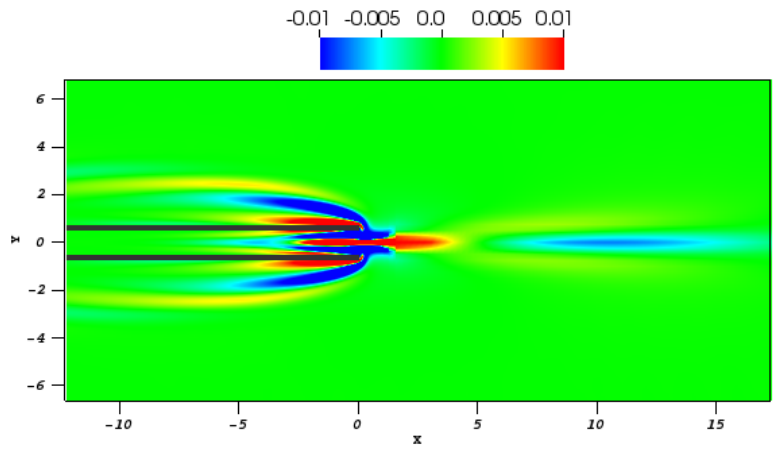

(a) Real part

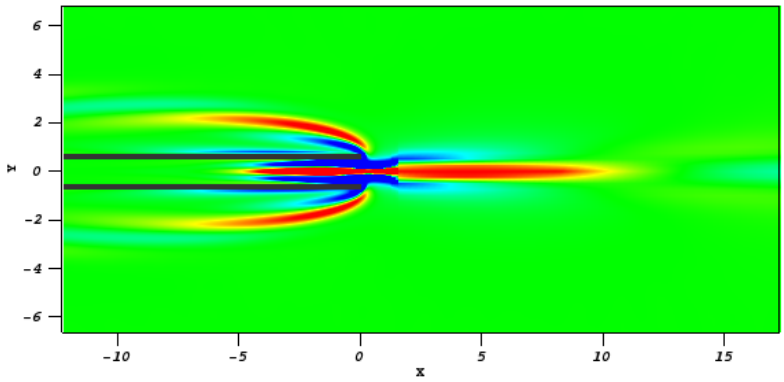

(b) Imaginary part

Figure 6.3. Vorticity contour of the adjoint mode obtained for the case of planar jet at $Re = 100$ and $\alpha = 1.1$.

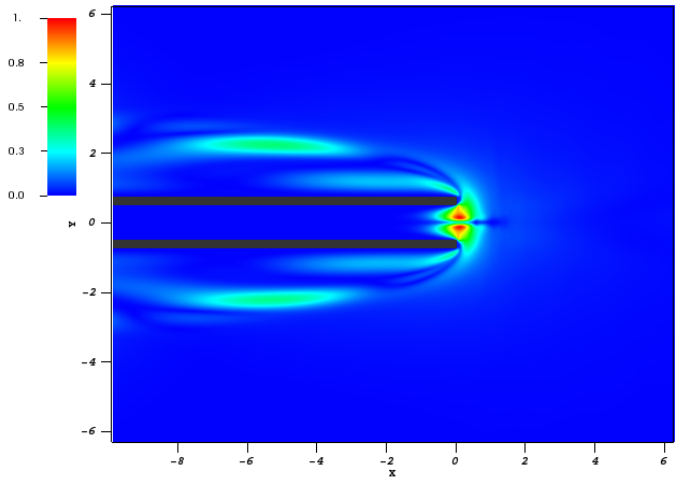

(a)

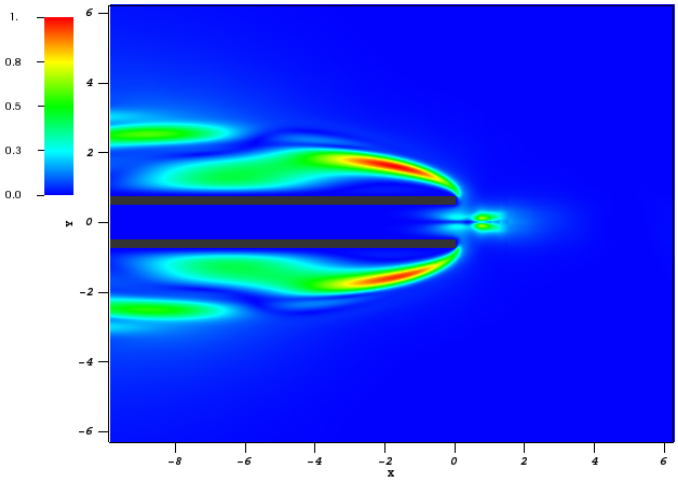

(b)

Figure 6.4. Wavemaker region obtained for planar jet at $Re = 100$ and $\alpha = 1.1$. (a) shows region where growth rate is most sensitive and (b) shows region where frequency is most sensitive.

It can be seen from figures (6.2) and (6.4) that the growth rate of the instability is sensitive to regions at the jet exit, while the frequency is sensitive to the regions around the pipe through which the jet is issued. The instability can be controlled by modifying the region around the jet exit.

6.2 Structural sensitivity of $Re = 50$ round jet at $\alpha = 3$

The three-dimensional structural sensitivity of the flowfield associated with a round jet at $Re = 50$ and $\alpha = 3$ is evaluated. The computational domain used for the analysis is described in section (4.2.1). Homogeneous Dirichlet boundary conditions are enforced on adjoint perturbations at all boundaries. The mesh used for the analysis is shown in figure (4.19).

All the computed modes for this configuration of the jet are found to be stable as shown in the figure (4.21). The leading adjoint mode is visualized in figure (6.5). The corresponding eigenvalue is found to be $-0.0281 \pm 0.346i$. The leading direct mode for this configuration is shown in figure (4.23) and the corresponding eigenvalue is $-0.0263 \pm 0.3448i$. The wavemaker region is visualized in figure (6.6). Forcing this region can enhance the instability and may even make this configuration unstable. This is especially important for mixing applications. However, the optimal forcing required to enhance the instability is not obtained in this research.

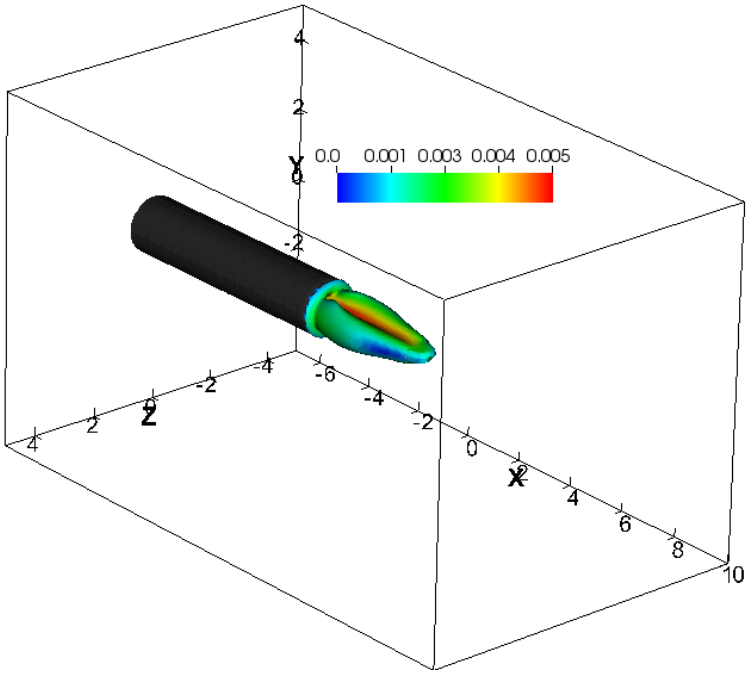

(a) Real part

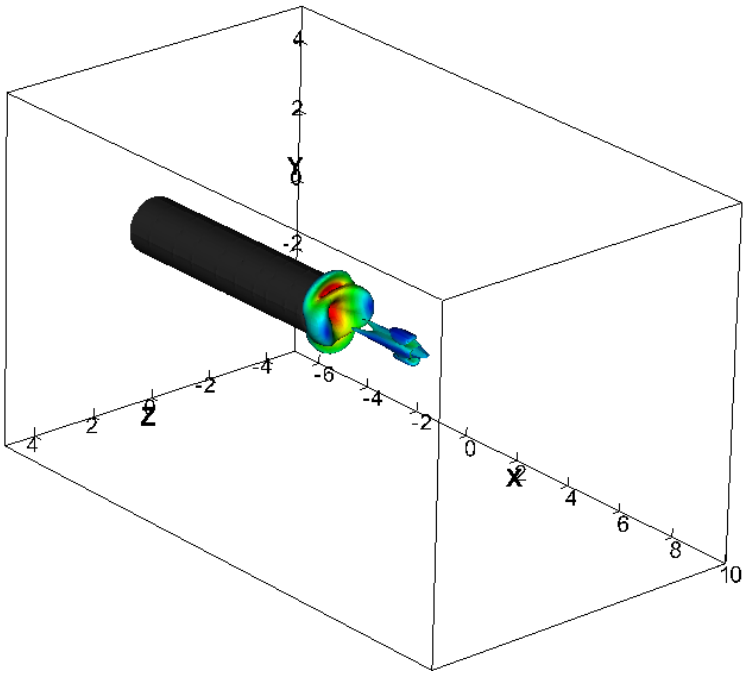

(b) Imaginary part

Figure 6.5. Isosurface of vorticity = 0.005 corresponding to the dominant eigenmode obtained for $Re = 50$ round jet at $\alpha = 3.0$. The isosurface is colored by the perturbation velocity magnitude.

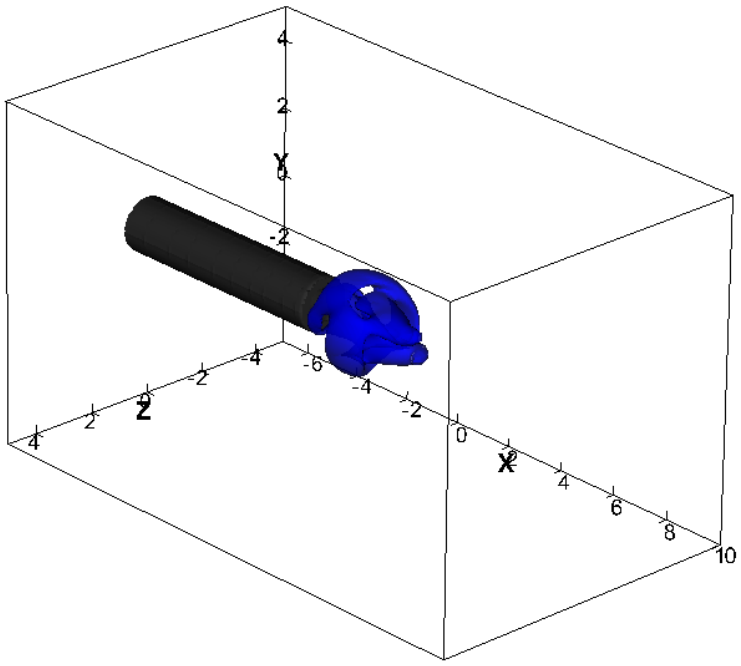

(a)

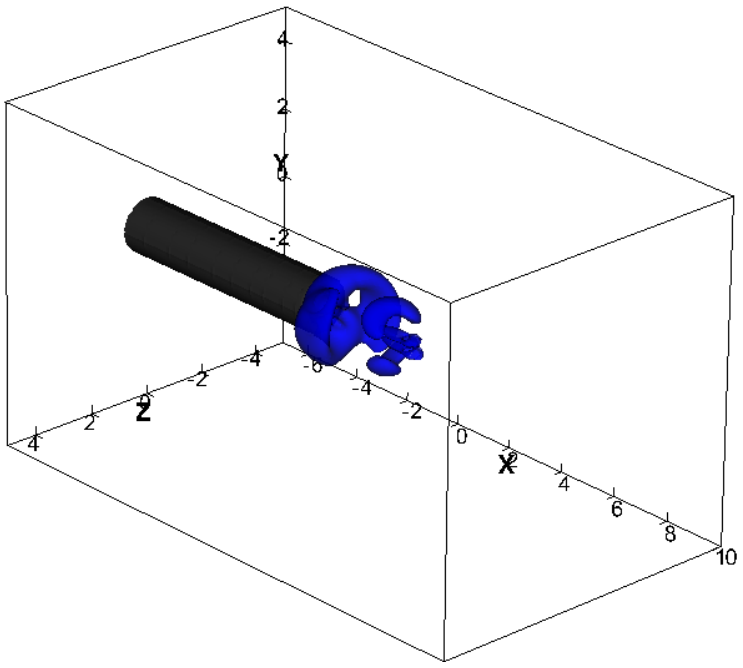

(b)

Figure 6.6. The wavemaker region for $Re = 50$ round jet at $\alpha = 3.0$ identified by the isosurface of $\delta\lambda = 0.25$.. (a) shows region where growth rate is most sensitive and (b) shows region where frequency is most sensitive.

6.3 Chapter summary

The sensitivity of the growth rate and the frequency of the eigenvalue corresponding to the dominant eigenmode to structural modifications in the base flow is obtained by computing the adjoint eigenmodes. The wavemaker region is obtained by overlapping the direct and adjoint modes and it is found to be specularly symmetric. In the case of two-dimensional planar jet at $Re = 50$ and $Re = 100$ at velocity ratio of 1.7 and 1.1 respectively, the growth rate is found to be sensitive to perturbations introduced at the jet exit. The frequency of the dominant eigenmode is most receptive to forcing introduced near the jet exit, around the pipe walls. The instability can be controlled by modifying the region around the jet exit. The wavemaker region in the case of round jet at $Re = 50$ at $\alpha = 3$ is found at region away from the jet exit, towards the base flow stagnation surface. By introducing optimal forcing at this location, the flowfield can be made unstable. This is beneficial for mixing applications.

CHAPTER 7

CONCLUDING REMARKS

7.1 Summary

In this thesis, stability analysis of the flowfield associated with a jet in counterflow was performed using linear hydrodynamic stability theory. The objective of this analysis was to understand the stability characteristics of the jet in presence of counterflow. The stability of two-dimensional planar jet and round jet was analyzed using numerical methods.

The mathematical formulation of the hydrodynamic stability theory was presented. The nonlinear Navier-Stokes equations, the linearized perturbation equations and the adjoint equations were solved using embedded boundary method. The computational meshes were dynamically adapted to the solution. Base flow solution was obtained using adaptive selective frequency damping (SFD) technique. However, it was found that SFD cannot be used to obtain base flows in the presence of unstable low frequency and stationary modes. In these cases, base flow was obtained using Newtons method. The search for global modes of instability was conducted using the block Krylov-Schur method.

The critical values of the jet Reynolds number, Re and the jet to counterflow velocity ratio, α that lead to instability were obtained from the eigenvalue analysis for the case of two-dimensional planar jet. At $Re = 50$, the critical α was found to be 1.6 while at $Re = 100$, the critical α is less than 1.1. The round jet was found to be stable at $Re = 50$ and $\alpha = 3$. At higher Reynolds numbers, shedding of axisymmetric

vortex rings was observed. For all the cases analyzed, the centrifugal modes that are at the low frequency end of the spectrum were found to be dominant.

The transient energy amplification of the perturbations was analyzed and the optimal initial conditions were analyzed. It was found that the non-normal effects of the Navier-Stokes operator are moderate at $Re = 50$ for both planar jet and round jet. The maximum energy growth obtained was less than two orders of magnitude. The non-normality effects become more prominent at $Re = 75$. The energy amplification factor at time horizon of 24 was found to be more than 500 at $\alpha = 1.1$ and it was found that the amplification for $\alpha = 1.1$ is greater than that for $\alpha = 1.3$. The optimal modes were found to be located near the jet exit and were found to be at the same spatial location at different time horizons. It was hypothesized that the transient growth mechanism arises from the compression of the jet column.

The regions in the flowfield where the growth rate and the frequency of the leading eigenvalue are most sensitive to structural modifications in the baseflow were identified from structural sensitivity analysis. For two-dimensional planar jet, it was found that the growth rate is sensitive to perturbations introduced at the jet exit while the frequency is most receptive to disturbances introduced near the jet exit, around the pipe walls. This shows the possibility of controlling the instability by modifying the region around the jet exit. For the round jet case, the wavemaker was located away from the jet exit, towards the base flow stagnation surface.

7.2 Future work

The analysis presented in this thesis can be extended to study the stability at higher jet Reynolds numbers and it is possible to find the critical parameters for the case of round jet. However, it was found that SFD technique is not applicable at

higher Reynolds numbers due to the presence of stationary modes. The base flow computation requires Newtons method.

In this research, it was found that the instability arises from streamline curvature. We expect the loss of stability of the two-dimensional base flow to three-dimensional perturbations as observed in the case of recirculating flows. This can be addressed by considering the effect of the spanwise periodic modes on the two-dimensional base flow stability.

The wavemaker region has been identified in this research. Passive flow control strategies such as placing a control cylinder, etc. can be evaluated by modifying the base flow structure at the wavemaker region. Finding the optimal forcing that has the most effect of the leading eigenvalue can provide even more valuable insights and can be beneficial for mixing applications.

The mechanism of instability was identified as centrifugal type. This can be confirmed by analyzing the streamline curvature as done in the case of other recirculating flows.

The effect of instability and the perturbations on scalar mixing from the jet can be quantified.

REFERENCES

[1] J. Arendt, H. A. Babcock and J. C. Schuster, "Penetration of a jet into counterflow," Proc. ASCE Journal Hydraulics Division, 82, 1956.

[2] S. Bernero, "A turbulent jet in counterow," PhD thesis, Technische Universitat Berlin, 2000.

[3] S. Beltaos and N. Rajaratnam, "Circular turbulent jet in an opposing infinite stream," First Canadian Hydraulics Conference, Edmonton, 1973.

[4] A. N. Sekundov, "The propagation of a turbulent jet in an opposing stream," Turbulent Jets of Air, Plasma, and Real Gas, Edited by G. N. Abramovich. Translated from Russian, New York: Consultants Bureau, 1969.

[5] W. D. Morgan, B. J. Brinkworth and G. V. Evans, "Upstream penetration of an enclosed counterflowing jet," Industrial and Engineering Chemistry Fundamentals, 15(2):125-127, 1976.

[6] M. Sivapragasam, M. D. Deshpande, S. Ramamurthy and P. White, "Turbulent Jet in Confined Counterflow," Sadhana 39, 713-729, 2014.

[7] M. Mahmoudi, "Investigation of the Velocity Field of Jets in Counter-Flow in the Vicinity of a Solid Wall", PhD thesis, University of Alberta, 2015.

[8] O. K*ö*nig and H. E. Fielder, "The structure of round turbulent jets in counterflow: a flow visualization study," Advances in turbulence, 3, 61-66, 1991.

[9] M. Yoda and H. E. Fielder, "The round jet in a uniform counterflow: flow visualization and mean concentration measurements," Experiments in Fluids, 21(6), 427-436, 1996.

[10] K. M. Lam, S. K. Tang and N. W. M. KO, "Instability of a circular jet in a weak opposing stream," Computational Mechanics, 1435-1439, 1991.

[11] K. M. Lam and H. C. Chan, "Investigation of turbulent jets issuing into a counterflowing stream using digital image processing," Exp. Fluids, 18, 210–222, 1995.

[12] D. F. Hopkins and J. M. Robertson, "Two-dimensional incompressible fluid jet penetration," Journal of Fluid Mechanics, 29, 273–287, 1967.

[13] L. Robillard and A. S. Ramamurthu, "Experimental Investigation of the Vortex Street Generated by a Plane Jet in a Counter Flow," ASME. J. Fluids Eng, 96(1), 43–48, 1974.

[14] K. M. Lam and H. C. Chan, "Round jet in ambient counterflowing stream," J. Hydraul. Eng., 123(10), 895-903, 1997.

[15] C. H. C. Chan and K. M. Lam, "Centerline velocity decay of a circular jet in a counterflowing stream," Physics of Fluids, 10, 637–644, 1998.

[16] S. Jendoubi and P. J. Strykowski, "Absolute and convective instability of axisymmetric jets with external flow," Physics of Fluids, 6, 3000–3009, 1994.

[17] S. Bernero and H. E. Fielder, "Experimental investigations of a jet in counterflow," Adv. Turbul. VII, 46, 35–38, 1998.

[18] S. Bernero and H. E. Fielder, "Application of particle image velocimetry and proper orthogonal decomposition to the study of a jet in a counterflow," Experiments in Fluids, 274-281, 2000.

[19] H. Tsunoda and M. Saruta, "Planar laser-induced fluorescence study on the diffusion field of a round jet in a uniform counter-flow," Journal of Turbulence, 4, N13, 2003.

[20] S. E. Elghobashi, G. S. Samuelsen, J. E. Wuerer, and J. C. LaRue, "Prediction and Measurement of Mass, Heat, and Momentum Transport in a Nonreacting

Turbulent Flow of a Jet in an Opposing Stream," Journal of Fluids Engineering 103(1), 127–132, 1981.

[21] C. Duwig and J. Revstedt, "Large Scale Dynamics of a Jet in a Counter Flow," Advances in Turbulence XII, (ed) B. Eckhardt, Springer Proceedings in Physics, 132. Springer, Berlin, Heidelberg, 2009.

[22] Z. H. Li, W. X. Huai and Z. D. Qian, "Large Eddy Simulation of a Round Jet into a Counterflow," Science China Technological Sciences 56 (2), 484–491, 2013.

[23] H. Jang and K. Mahesh, "Large eddy simulation of flow around a reverse rotating propeller," Journal of Fluid Mechanics, 729, 151-179, 2013.

[24] M. Gharib, E. Rambod and K. Shariff, "A universal time scale for vortex ring formation," Journal of Fluid Mechanics, 360, 121–140, 1998.

[25] J. O. Dabiri and M. Gharib, "Delay of vortex ring pinchoff by an imposed bulk counterflow", Physics of Fluids, 16(4), 2004.

[26] O. Reynolds, "An experimental investigation of the circumstances which determine whether the motion of water shall be direct or sinuous, and of the law of resistance in parallel channels," Phil. Trans. of the Royal Soc. 174, 935-982, 1884.

[27] Lord Rayleigh, "On the instability of jets," Proceding of the London Mathematical Society, 10, 4–13, 1879.

[28] Lord Rayleigh, "On the stability, or instability, of certain fluid motions," Proceedings of the London Mathematical Society, 11, 57-70, 1880.

[29] W. M. Orr, "Lord Kelvin's investigations, especially the case of a stream which is shearing uniformly," Proceedings Royal Irish Academy, A27, 80–138, 1907. o

[30] W. M. Orr, "The stability or instability of the steady motions of a perfect liquid and of a viscous liquid," Proceedings Royal Irish Academy, A27, 9–138, 1907.

[31] A. Sommerfeld, "Ein beitraz zur hydrodynamischen erklaerung der turbulenten fluessigkeitsbewegungen," Proc. Fourth Inter. Congr. Mathematicians, Rome, 116–124, 1908.

[32] R. Briggs, "Electron-Stream Interaction with Plasmas," MIT Press, 1964.

[33] A. Bers, "Linear waves and instabilities," in Physique des Plasmas (ed. C. DeWitt and J. Peyraud), Gordon and Breach, 113–215, 1975.

[34] P. Huerre and P. A. Monkewitz, "Absolute and convective instabilities in free shear layers," Journal of Fluid Mechanics, 159, 151-168, 1985.

[35] W. Koch, "Local instability characteristics and frequency determination of self-excited wake flows," J. Sound Vib., 99, 5383, 1985.

[36] J.-M. Chomaz, P. Huerre and L. G. Redekopp, "Bifurcations to local and Global modes in spatially-developing flows," Phys. Rev. Lett., 60, 25-28, 1988.

[37] P. Huerre and P. A. Monkewitz, "Local and global instabilities in spatially developing flows," Annu. Rev. Fluid Mech., 22, 473-53, 1990.

[38] C. M. Bender and S. A. Orszag, "Advanced Mathematical Methods for Scientists and Engineers," New York: McGraw-Hill, 1978.

[39] S. Bagheri, P. Schlatter, P. J. Schmid and D. S. Henningson, "Global stability of a jet in crossflow," Journal of Fluid Mechanics, 624, 33-44, 2009.

[40] L. Massa, "Mach number effects on the global mixing modes induced by ramp injectors in supersonic flows," Journal of Fluid Mechanics, 757, 403-431, 2014.

[41] V. A. Romanov, "Stability of plane-parallel Couette flow," Functional Anal. Applics., 7, 137-146, 1973.

[42] P. J. Schmid and L. Brandt, "Analysis of fluid systems: stability, receptivity, sensitivity," Appl. Mech. Rev., 66 (2), 1-21, 2014.

[43] P. J. Schmid and D. S. Henningson, "Stability and Transition in Shear Flows," Springer-Verlag, New York, 2001.

[44] K. M. Butler and B. F. Farrell, "Three-dimensional optimal perturbations in viscous shear flows," Phys. Fluids A, 4, 1637-1650, 1992.

[45] C. Cossu and J.-M. Chomaz, "Global measures of local convective instabilities," Phys. Rev. Lett., 78 (23), 4387-4390, 1997.

[46] P. J. Schmid, "Nonmodal stability theory," Annual Review of Fluid Mechanics, 39, 129-162, 2007.

[47] L. N. Trefethen, A. E. Trefethen, S. C. Reddy and T. A. Driscoll, "Hydrodynamic stability without eigenvalues," Science, 261, 578-584, 1993.

[48] L. N. Trefethen and M. Embre, "Spectra and Pseudospectra," Princeton University Press, Princeton.

[49] D. C. Hill, "Adjoint systems and their role in the receptivity problem for boundary layers," Journal of Fluid Mechanics, 292, 183-204, 1995.

[50] A. Tumin, "The biorthogonal eigenfunction system of linear stability equations: a survey of applications to receptivity problems and to analysis of experimental and computational results," AIAA Paper 2011–3244, 2011.

[51] J.-M. Chomaz, "Global instabilities in spatially developing flows: non-normality and nonlinearity," Annu. Rev. Fluid Mech., 37, 357-392, 2005.

[52] P. J. Strykowski and K. R. Sreenivasan, "On the formation and suppression of vortex shedding at low reynolds numbers," Journal of Fluid Mechanics, 218, 71-107, 1990.

[53] D. C. Hill, "A theoretical approach for analyzing the re-stabilization of wakes," AIAA Paper,92-0067, 1992.

[54] F. Giannetti and P. Luchini, "Structural sensitivity of the first instability of the cylinder wake," Journal of Fluid Mechanics, 581, 167-197, 2007.

[55] P. Luchini and A. Bottaro, "Adjoint Equations in Stability Analysis," Annual Review of Fluid Mechanics, 46, 493-517, 2014.

[56] V. Theofilis, "Global linear instability," Annual Review of Fluid Mechanics, 43, 319-352, 2011.

[57] D. Sipp, O. Marquet, P. Meliga and A. Barbagallo, "Dynamics and control of global instabilities in open flows: a linearized approach," Applied Mechanics Review, 63, 030801, 2010.

[58] D. Barkley, H. M. Blackburn, S. J. Sherwin, "Direct optimal growth analysis for timesteppers," Int. J. Numer. Methods Fluids, 57, 1435-1458, 2008.

[59] P. Colella, D. T. Graves, T. J. Ligocki, G. H. Miller, D. Modiano, P. O. Schwartz, B. Van Straalen, J. Pillod, D. Trebotich and M. Barad, "EBChombo Software Package for Cartesian Grid, Embedded Boundary Applications," Lawrence Berkeley National Laboratory Technical Report LBNL-6615E, 2014.

[60] D. Trebotich and D. T. Graves, "An adaptive finite volume method for the incompressible NavierStokes equations in complex geometries," Communications in Applied Mathematics and Computational Science, 10(1), 43-82, 2015.

[61] Q. Liu, J. M. Prez, F. Gmez and V. Theofilis, "Instability and sensitivity analysis of flows using OpenFOAM," Chinese J. Aeronautics 29 (2), 316-325, 2016.

[62] M. L. Minion, "On the stability of Godunov-projection methods for incompressible flow," J. Comput. Phys., 123, 435–449, 1996.

[63] A. Almgren, J. Bell, P. Collella, L. Howell, and M. Welcome, "A conservative adaptive projection method for the variable density incompressible Navier-Stokes equations," J. Comput. Phys., 142, 1-46, 1998.

[64] E. H. Twizell, A. B. Gumel and M. A. Arigu, "Second-order, l_0–stable methods for the heat equation with time-dependent boundary conditions," Advances in Computational Mathmatics, 6, 333-352, 1996.

[65] L. S. Tuckerman and D. Barkley, "Bifurcation analysis for timesteppers," Numerical methods for bifurcation problems and large-scale dynamical system, 453–566, 2000.

[66] P. Colella, D. T. Graves, T. J. Ligocki, D. F. Martin, D. Modiano, D. B. Serafini, B. V. Straalen, "CHOMBO software package for AMR applications: design document," Technical report, Lawrence Berkeley National Laboratory, Applied Numerical Algorithms Group; NERSC Division; Berkeley, CA, USA, 2003

[67] E. Åkervik, L. Brandt, D. Henningson, J. Hoepffner, O. Marxen and P. Schlatter, "Steady solutions of the Navier-Stokes equations by selective frequency damping," Physics of Fluids, 18, 2006.

[68] B. E. Jordi, C. J. Cotter and S. J. Sherwin, "Encapsulated formulation of the selective frequency damping method," Physics of Fluids, 26(3), 034101, 2014.

[69] B. E. Jordi, C. J. Cotter and S. J. Sherwin, "An adaptive selective frequency damping method," Physics of Fluids, 27, 094104, 2015.

[70] T. E. Oliphant, "Python for Scientific Computing," Computing in Science and Engineering, 9, 10–20, 2007.

[71] G. Cunha, P. Y. Passaggia and M. Lazareff, "Optimization of the Selective Frequency Damping parameters using model reduction," Physics of Fluids, 27, 094103, 2015.

[72] C. G. Baker, U. L. Hetmaniuk, R. B. Leheoucq and H. K. Thornquist, "Anasazi software for the numerical solution of large-scale eigenvalue problems," ACM Transactions on Mathematical Software (TOMS), 36(3), 1–23, July 2009.

[73] R. B. Lehoucq, D. C. Sorensen and C. Yang, "ARPACK User's Guide: Solution of Large-Scale Eigenvalue Problems with Implicitly Restarted Arnoldi Methods," SIAM, 1998.

[74] G. W. Stewart, "A Krylov-Schur algorithm for large eigenproblems," SIAM J. Matrix Anal. Appl., 23, 601–614, 2002.

[75] X. Garnaud, L. Lesshaft, P. J. Schmid and J. M. Chomaz, "A relaxation method for large eigenvalue problems, with an application to flow stability anlaysis," J. Comp. Phys., 231(10), 3912-3927, 2012.

[76] D. Barkley, "Linear analysis of the cylinder wake mean flow", EPL (Europhysics Letters), 75(12), 2006.

[77] D. Barkley, G. M. Gomes and R. D. Henderson, "Three-dimensional instability in flow over a backward-facing step," Journal of Fluid Mechanics, 473, 167-190, 2002.

[78] G. A. Brès and T. Colonius, "Three-dimensional instabilities in compressible flow over open cavities," Journal of Fluid Mechanics, 599, 309-339, 2008.

BIOGRAPHICAL STATEMENT

Siddarth Chintamani was born in Visakhapatnam, India in 1990. He obtained his bachelors degree in Mechanical Engineering from PES University, Bangalore, India in 2012. He has spent five years as a graduate student at University of Texas at Arlington, working under Dr. Brian Dennis and Dr. Luca Massa. During his graduate studies, he worked on developing chemically reactive flow solver, embedded boundary methods, hp-refinement methods, vortex dynamics, global stability of jet flows and scramjet injectors.

His research interests include effects of Damkholar number of global stability of fluid flows, vortex dynamics, reduced order modeling and high performance computing. He worked as a graduate research assistant from 2012-2014 and has been a graduate teaching assistant since 2014. He is a student member of AIAA and ASME.